



# Water vapor line profile at 183-GHz: Temperature dependence of broadening, shifting, and speed-dependent shape parameters

M.A. Koshelev<sup>a,\*</sup>, I.N. Vilkov<sup>a</sup>, D.S. Makarov<sup>a</sup>, M.Yu. Tretyakov<sup>a</sup>, B. Vispoel<sup>b,c,d</sup>, R.R. Gamache<sup>b</sup>, D. Cimini<sup>e</sup>, F. Romano<sup>e</sup>, P.W. Rosenkranz<sup>f</sup>

<sup>a</sup> Institute of Applied Physics RAS, 46 Ul'yanov Street, Nizhny Novgorod 603950, Russia

<sup>b</sup> Department of Environmental, Earth, and Atmospheric Sciences, University of Massachusetts Lowell, Lowell, MA 01854, USA

<sup>c</sup> Research Unit Lasers and Spectroscopies (LLS), Institute of Life, Earth and Environment (ILEE), University of Namur (UNamur), 61 rue de Bruxelles, Namur, B-5000, Belgique

<sup>d</sup> Royal Belgian Institute for Space Aeronomy (BIRA-IASB), 3 Avenue Circulaire, Brussels 1180, Belgium

<sup>e</sup> National Research Council of Italy, Institute of Methodologies for Environmental Analysis, Potenza 85050, Italy

<sup>f</sup> Massachusetts Institute of Technology, Cambridge, MA 02139, USA



## ARTICLE INFO

### Article history:

Received 25 September 2020

Revised 4 December 2020

Accepted 7 December 2020

Available online 11 December 2020

### Keywords:

Microwave laboratory spectroscopy  
Modified complex Robert–Bonamy calculations

Radiative transfer modeling  
Speed-dependent profile  
Water vapor  
Line shape parameters

## ABSTRACT

The water vapor line at 183 GHz was studied over the temperature range of 219–358 K using a spectrometer with radioacoustic detection of absorption, providing a signal-to-noise ratio of up to 8000. The study includes the first measurement of speed-dependent collisional broadening and shifting of this line for both self- and air-broadening, and their temperature dependences. The sign of self-shifting changes at about 280 K. Line-shape parameters are obtained for Voigt and quadratic speed-dependent Voigt shape factors. Temperature dependences of the line parameters are analyzed using empirical models from the literature. Theoretical Modified Complex Robert–Bonamy calculations of the line shape parameters, their temperature and speed-dependence are made over the temperature range of 200–3000 K. The measurements and calculations show very good agreement, although with some discrepancies for line shift parameters. The impact of the newly-measured line parameters on atmospheric water-vapor estimation from ground-based and satellite instruments is evaluated by simulation of downwelling and upwelling brightness temperatures and retrieved water-vapor mixing ratio, for atmospheric conditions typical of six climate zones. For the case of ground-based or limb-scanning radiometry with a background of cold space, the impact of speed-dependence is comparable to or exceeds that of measurement error and will introduce systematic errors if neglected. Therefore, consideration of speed-dependence is necessary for accurate estimation of water vapor with this line. The impact on upwelling brightness temperature is smaller.

© 2020 Elsevier Ltd. All rights reserved.

## 1. Introduction

The 183-GHz water vapor line corresponding to the pure rotational transition  $J'_{K_a,K_c} - J_{K_a,K_c} = 3_{1,3} - 2_{2,0}$  is one of the two most important microwave atmospheric diagnostic lines used in atmospheric water vapor remote sensing.

Microwave radiometry at 183 GHz is used for water-vapor sensing from ground-based, airborne, and satellite sensors. Ground-based sensors include the Ground-based Scanning Radiometer (GSR, Cimini et al. [1]), the G-band Vapor Radiometer Profiler (GVRP, Cadeddu et al. [2]), and the H<sub>2</sub>O Antarctica Microwave

Stratospheric and Tropospheric Radiometers (HAMSTRAD, Ricaud et al. [3]). Airborne sensors include the Conical Scanning Millimeter-wave Imaging Radiometer (CoSMIR, Wang et al. [4]), and the High Altitude LOng range research aircraft (HALO) with Microwave Package (HAMP, Mech et al. [5]). Operational satellite measurements at 183.31 GHz started in 1991 [6], and exhibit good overlap and continuity since the early 1990's to the present, both from imager and sounder sensors. These include the Advanced Microwave Sounding Unit-B (AMSU-B), the Microwave Humidity Sounders (MHS), the Advanced Technology Microwave Sounder (ATMS), the Special Sensor Microwave Imager Sounder (SSMIS), the Global Precipitation Mission's Microwave Imager (GMI), the Sondeur Atmosphérique du Profil d'Humidité Intertropicale par Radiométrie (SAPHIR), the Microwave Limb Sounder (MLS), the Micro-Wave Humidity Sounder (MWHS), and the advanced

\* Corresponding author.

E-mail address: [koma@ipfran.ru](mailto:koma@ipfran.ru) (M.A. Koshelev).

microwave imager/sounder (MTVZA-GY-MP). This record will continue with future sensors, such as the Microwave Imager (MWI), the Microwave Sounder (MWS), and the Ice Cloud Imager (ICI) instruments onboard the second generation of European polar satellite mission (MetOp-SG), planned to measure until 2045. The 183-GHz line is also exploited in recent missions demonstrating microwave radiometer observations from centimeter-size satellites [7,8]. All of the above radiometers measure radiation intensity at selected frequencies around the center of the 183-GHz line to infer atmospheric water vapor profiles. Observations at 183 GHz are also widely used to feed state-of-the-art numerical weather prediction (NWP) models, showing significant impact [9]. As part of their quality control, radiometric observations are often validated against simulated radiances obtained by processing thermodynamic profiles from radiosondes or NWP models with a radiative transfer (RT) model [10,11]. Such a validation is affected by systematic uncertainty on both the observations and simulations [12], with the RT model contribution estimated to be of the same order as instrumental accuracy [13]. Reducing the RT uncertainty would allow for better validation and thus use of 183-GHz global observations. This calls for the continuous refinement of spectroscopic parameters [14] and absorption models [15], as well as the rigorous characterisation of their uncertainties [16].

Thus a thorough individual approach to the study of the line is required for accurate and comprehensive knowledge of the line shape, its numerical parameters including intensity, pressure broadening and shifting parameters, and their speed-dependence and their temperature behavior. The most complete to date information on the line parameters is collected in the review paper of Tretyakov [14]. It was noted in Tretyakov [14] that among collisional parameters, only air-broadening of the line related to the Voigt, Lorentz or Van Vleck–Weisskopf form factors is known with uncertainty less than 1%. The less-studied parameters of the line are pressure shifting and temperature dependence of the line broadening and shifting parameters. The influence of the effect of speed-dependence of collisional relaxation rate on the line shape has never been studied for the 183-GHz line and it is not taken into account in the models of atmospheric absorption of microwave radiation. In the infrared, the line shape distortion due to this effect can reach a few percent of the peak absorption, limiting the line shape modeling accuracy [17,18].

In the present study, we revise the 183-GHz line shape parameters in a temperature range relevant to the atmosphere, from 219 to 358 K, using a spectrometer with radio-acoustic detection of the absorption signal (RAD spectrometer [19]). The signal-to-noise ratio (SNR) of the recorded spectra was up to 8000, which allowed accurate measurement of the speed-dependent broadening and shifting coefficients and their temperature dependences. It was shown for the first time that the self-shifting parameter of the 183-GHz line changes its sign from negative to positive as temperature increases above 280 K. The experimental study of the line is complemented by theoretical calculation of its collisional parameters by the Modified Complex Robert–Bonamy method [20], performed over the temperature range of 200–3000 K and demonstrating good agreement with the measured data. Expressions for modeling of the temperature behavior of the 183-GHz water line-shape parameters are discussed.

Experimental details are presented in Section 2. Section 3 concerns line shape models used for the spectra analysis and corresponding parameters retrieval. In Section 4 we discuss theoretical formalism and results of supporting calculations. Section 5 is devoted to analysis of temperature dependences of obtained parameters. Evaluation of the impact of the new line parameters on radiative transfer modeling and water vapor retrievals by use of ground-based and satellite instruments is given in Section 6. Closing remarks are collected in Section 7.

## 2. Experimental details

The spectrometer with a backward-wave oscillator and a radio-acoustic detection of absorption was employed. The spectrometer and measurement method is similar to that used in our earlier study of the temperature dependence of line-shape parameters of oxygen fine-structure lines in the millimeter-wave region [21]. More technical and methodological information can be found in Refs. [22–24]. Some particular details follow. The compact copper gas cell (~10 cm length, ~2 cm diameter) with a sensitive microphone was permanently connected with the thermostat (model LOIP FT-311-80, Russia) which provides temperature of a coolant inside the thermostat in the range from 193 to 373 K, with stability of ±0.1 K around the chosen value. The cell was additionally isolated from the ambient atmosphere by a polyethylene-foam case. Four copper temperature sensors of ±0.5 K stated uncertainty were mounted on the cell surface. Temperature gradients were estimated to be zero at room temperature, increasing up to 0.5 K at the limits of the operating range. Gas pressure in the cell was permanently monitored using two pressure gauges: 10-Torr range (MKS Baratron type 626B) and 100-Torr range (Pfeiffer Baratron model CCR-362), whose readings coincided within the declared inaccuracies of 0.25% and 0.2% of reading, respectively. A sample of natural double-distilled water, degased by freezing and pumping, was used for the study. The dry air sample was preliminarily prepared as a mixture of high purity (better than 99.99%) gases of nitrogen, oxygen and argon in natural abundance, constituting 78%, 21% and 1%, respectively. Temperature stability within ±0.5 K of the whole setup during each experimental day was provided by the room air conditioning. A short summary of the experimental conditions is given in Table 1.

The measurement procedure was as follows. The cell temperature was set and kept constant overnight before the experiment. Prior to the experiment the cell was pumped down to  $10^{-5}$  Torr or less by a turbomolecular pump. At a given temperature, spectra were recorded at 8–10 pressures. In the case of self-broadening, we started from 0.023 Torr. The maximum pressure value depended on the water vapor saturation pressure and varied from 0.7 Torr at 358 K down to 0.15 Torr at 238 K. In the case of air-broadening, the partial pressure of water in the mixture was set from 0.012 to 0.09 Torr. Then foreign gas was gradually added into the cell by steps of 0.2–0.3 Torr, and the line recording started after achieving equilibrium, which was controlled by monitoring the time variation of the line's peak absorption. The corresponding time was experimentally estimated to be about 30–60 min depending on the water content in a mixture. Each spectrum was recorded at 200 frequency points within an interval of about 30 line half-widths around its center, which allowed accurate line shape analysis and instrumental baseline determination. To get the “true” line shape, modulation of radiation power at 80 Hz and synchronous detection of the signal was used. A typical line recording is shown in Fig. 1.

To improve precision and estimate the statistical uncertainty of the line shape parameters, several forward and backward spectra recordings were obtained at each pressure and then analyzed separately. The line shape distortion due to standing waves in the

**Table 1**

Summary of the experimental conditions for the self- and air-pressure broadening study.

Perturber	Parameter	Parameter range	Number of spectra
$H_2O$	$P_{water}$ , Torr	0.012–0.638	595
	T, K	238–358	
Air	$P_{water}$ , Torr	0.004–0.089	857
	$P_{air}$ , Torr	0.038–1.583	
	T, K	219–358	

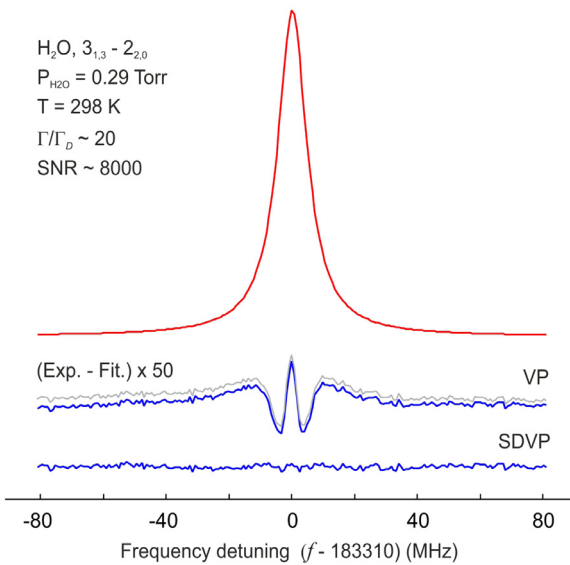


**Fig. 1.** Typical line recording of the 183-GHz water line at 298 K and 0.29 Torr of pure water. Zoomed-in 50 times residuals (Exp.-Fit.) for VP and qSDVP models are shown in the lower part of the figure. The difference between VP residuals (blue and grey) corresponds to the baseline contribution. Ratio of collisional to Doppler width  $\Gamma/\Gamma_D$  is 20. Signal-to-noise ratio of the recording is about 8000 for qSDVP.

spectrometer waveguide path was reduced by averaging line parameters obtained from the spectra recorded at several different positions of the cell relative to the radiation source (different interference patterns). This method decreases the precision of the data, but increases the accuracy due to the effective averaging of the influence of the standing waves.

### 3. Line-shape models and spectra analysis

The experimental spectra analysis started with the conventional Voigt profile (VP) taking into account both Doppler and collisional broadening. The Doppler half-width at half maximum (HWHM)  $\Gamma_D$  at a temperature  $T$  was calculated as  $\Gamma_D = 15.472\sqrt{T}$  (in MHz,  $T$  in Kelvin) and fixed in the model function. The spectrometer baseline was modeled by a polynomial function of up to second order in frequency, depending on pressure and linewidth [22]. The parameters of the baseline polynomial were determined together with the line-shape parameters from the fit of the model function to the experimental recording. An example of the fit residual for the Voigt profile is given in Fig. 1. The contribution of the instrumental baseline is shown in the VP residual, demonstrating its smallness. The figure also demonstrates that the observed line cannot be reproduced to within the noise level by the Voigt profile. However, the Voigt parameters will be presented and discussed here because they can be directly compared with previous data and used in radiation propagation codes without any modification of the line-shape function.

Two physical effects related to molecular collisions, namely, velocity changing collisions (Dicke effect) and speed-dependence of collisional relaxation (SD-effect) are considered to be responsible for the observed discrepancy from the Voigt shape. However, it has been shown in our earlier studies for different molecules, such as OCS [25], CO [26], H<sub>2</sub>O [24], and O<sub>2</sub> [27], that under conditions of our experiments collisional broadening prevails and the SD-effect dominates the line shape deviation, while the Dicke effect makes no noticeable contribution to the shape of the observed lines. Therefore, further data analysis was performed using the quadratic speed-dependent Voigt profile (qSDVP) in the Hartmann-Tran implementation [28]. The model takes into account

speed-dependence of collisional width  $\Gamma(\nu)$  and shift  $\Delta(\nu)$  using the quadratic law proposed by Rohart et al. [29]:

$$\Gamma(\nu) + i\Delta(\nu) = \Gamma_0 + i\Delta_0 + (\Gamma_2 + i\Delta_2) \cdot \left[ \left( \frac{\nu}{\tilde{\nu}} \right)^2 - \frac{3}{2} \right], \quad (1)$$

where  $\nu$  is the speed and  $\tilde{\nu} = \sqrt{2k_B T/m}$  is the most probable speed of an absorbing (active) molecule of mass  $m$ . The fit residual shown in Fig. 1 demonstrates complete correspondence of the model function to the experimental data.

A line-by-line approach was used for the data analysis, which implied separate adjustment of each parameter of the line model at each pressure and temperature. The slight manifestation of the transition saturation effect by radiation intensity  $W$  was taken into account. The effect causes increasing collisional line half-width as  $\Gamma(W) = \sqrt{\Gamma(0)^2 + \nu_R^2(W)}$ , where  $\nu_R$  is the Rabi frequency and  $\Gamma(0)$  is the half-width of the unsaturated line, linearly depending on pressure [30]. The radiation intensity is known only approximately and constitutes about 5–6 mW/cm<sup>2</sup>. Moreover, it depends on the position of the gas cell relative to the radiation source and slightly varies from day to day. For each series of line broadening measurements corresponding to some certain position of the cell the Rabi frequency was used as an adjustable parameter. Typical values constituted about 0.25–0.3 MHz, which is in agreement with the value 0.26–0.29 MHz calculated as  $\nu_R = d \cdot E/h$  [31], where  $E$  is the amplitude of the electric field of the radiation,  $h$  is the Planck constant, and  $d = 0.265$  D [32] is the matrix element of the dipole moment of the transition. The contribution of the saturation effect to the line width, retrieved in this way, was subtracted for proper representation of the collisional broadening. Typical pressure-dependences of the line parameters obtained from the fit of a line shape model at three temperatures within the studied range are presented in Fig. 2. The pressure-normalized broadening and shifting coefficients ( $\gamma, \delta$  for VP and  $\gamma_0, \gamma_2, \delta_0, \delta_2$  for qSDVP) were retrieved by linear approximation of the experimental points. Their temperature dependence is analyzed in Section 5.

Fig. 3 demonstrates the large amount of single line recordings performed in the course of this work for the determination of line parameters. Each point corresponds to the collisional half-width  $\Gamma_0(296)$  of the line retrieved from a spectrum similar to the one shown in Fig. 1 and plotted versus pressure of perturbing gas. All data were recalculated to 296 K using the equations discussed in Section 5. In the case of air broadening, the calculated contribution of the self-broadening was subtracted from the line width. The larger spread of points in comparison with a single pressure ramp experiment (Fig. 2) is due to the influence of the spectrometer baseline (standing waves). For air-broadening additional uncertainty can be caused by adsorption/desorption processes in the gas cell. The slopes of the lines fitted to all these data yielded 20.027(12) and 4.033(4) MHz/Torr for the self- and air-broadening, respectively, in good agreement with corresponding experimental values reported for 296 K in Section 5.2.

## 4. Theoretical formalism and computations

### 4.1. Modified semi-classical Robert–Bonamy theory

The calculations of the half-width and line shift were made using the complex implementation of the Modified semi-classical Robert–Bonamy theory [20] and is designated MCRB. In this formalism the half-width,  $\Gamma$  and line shift,  $\Delta$ , for a ro-vibrational transition  $f \leftarrow i$  of active molecule can be written in terms of the collisional cross-sections  $\sigma_{Re}$  and  $\sigma_{Im}$ :

$$(\Gamma(\nu_{rel}) - i\Delta(\nu_{rel}))_{f \leftarrow i} = \frac{\rho}{2\pi} \nu_{rel} (\sigma_{Re} - i\sigma_{Im}) \quad (2)$$

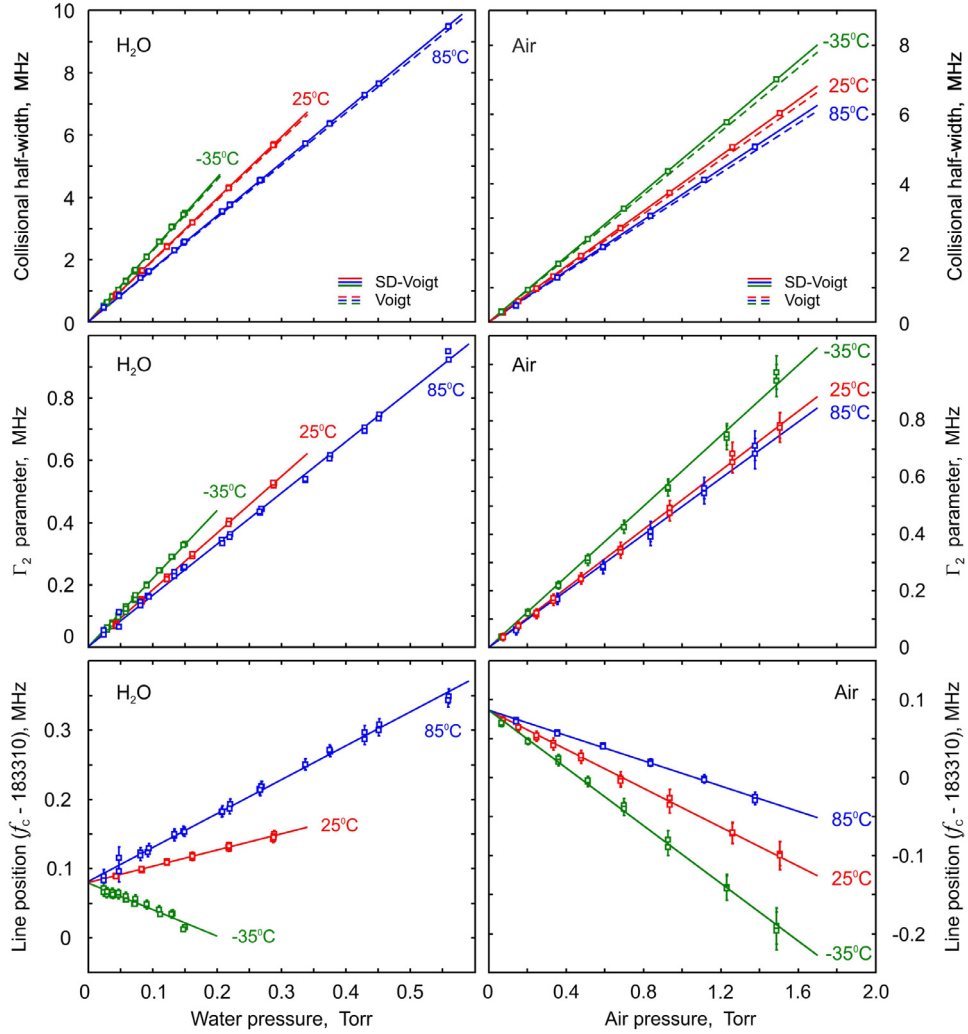


**Fig. 2.** Dependence of collisional half-width (upper panels), speed-dependence  $\Gamma_2$  parameter (middle panels) and line center position (lower panels) on pressure of water (left) and air (right) at three temperatures (shown near the corresponding lines). Error bars correspond to  $\pm 3\sigma$  uncertainty determined from the line-shape fitting. Dashed lines in the upper panels correspond to the VP parameter  $\Gamma$ , solid lines to the qSDVP parameter  $\Gamma_0$ . The contribution of self-broadening and self-shifting was subtracted from the corresponding air data.

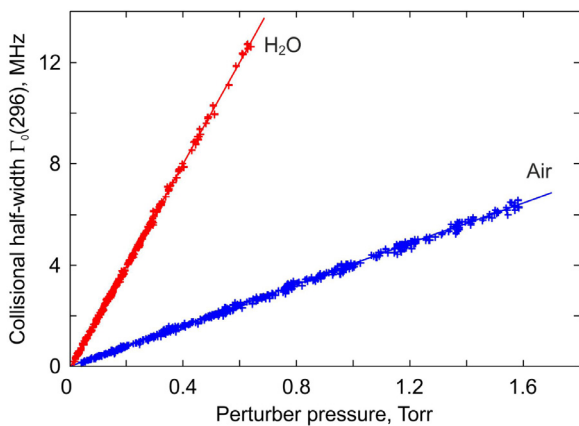


**Fig. 3.** Collisional half-width  $\Gamma_0(296)$  as a function of pressure of perturbing gas. Points (crosses) are data obtained from all recorded spectra recalculated to 296 K using the power law (8) and parameters from Table 5. Lines are the result of linear regression of experimental points. Uncertainties are not displayed for figure clarity.

where  $\rho$  is the number density of the perturbers (collision partner of active molecule), and  $v_{rel}$  is the mean relative thermal velocity. The collisional cross-sections are given by

$$\sigma_{Re} - i\sigma_{Im} = \int_0^\infty 2\pi b [1 - e^{-i(S_1 + Im(S_2))J_2} e^{-(Re(S_2))J_2}] db \quad (3)$$

where  $\langle \rangle_{J_2}$  is an average over the states of the perturber, and  $b$  is the impact parameter. The first and second order terms in the successive expansion of the Liouville scattering matrix,  $S_1$  and  $S_2$ , depend on the ro-vibrational states of the transition, the associated collisionally-induced jumps from these states, on the intermolecular potential, and the characteristics of the collision dynamics. The formalism has been described in a number of publications [33–35] and only a summary is presented here. Interested readers can refer to the original articles.

The MCRB formalism is a semi-classical method to determine the line shape parameters. Semi-classical designates that the internal structure of the colliding molecules is treated via quantum mechanics and the dynamics of the collision process are determined via classical mechanics. Thus, in an optical transition from initial to final state, the active molecule will undergo collisions with the perturbing (bath) molecules, for which the trajectories of motion are determined using Hamilton's equations. In these collisions, the ini-

tial and final states of the active (radiating) molecule,  $i$  and  $f$ , and perturbing molecule,  $J_2$ , will undergo collisionally induced transitions to states  $i'$ ,  $f'$ ,  $J'_2$  interrupting the radiation and causing collisional broadening. The states  $i'$  and  $f'$  are called the collisionally connected states of the radiator and the states  $J_2$  and  $J'_2$  are called the collisionally connected states of the perturber. These collisionally induced transitions are given by selection rules determined by the wavefunctions and the intermolecular potential. Given the large number of terms in the intermolecular potential used in this work, there are many states,  $i'$  or  $f'$  or  $J'_2$ , that are possible. The quantum mechanical components of the calculation are the energies of the states involved in the collisionally induced transitions and the wavefunctions for these states, which are used to determine the probability of a collisionally induced transition for the radiator and perturber molecules. This probability is given by a reduced matrix element [33,36,37].

In the MCRB formalism the intermolecular potential consists of complex-valued electrostatic, atom-atom, induction, and London dispersion terms [38]. The electrostatic and atom-atom components are effective at intermediate and close internuclear separations, respectively. The induction, and London dispersion terms (the  $S_1$  term) are important for determining the line shift but also have a noticeable contribution to the half-width. The electrostatic, induction, and dispersion terms are given by functional forms with numerical scaling factors given in terms of molecular constants such as dipole and quadrupole moments, polarizabilities, ionization potentials, etc. The main uncertainties lie in the vibrational dependence of the dipole moment (induction) and polarizability (dispersion) and in the parameters of the atom-atom potential. However, for water vapor, the parameters for the vibrational dependence of the dipole moment [39] and polarizability [40] are known and used in this work. What remains is to determine a reasonable set of atom-atom constants.

Gamache and Fischer [41] have shown that for some collision systems a relatively small adjustment in the atom-atom parameters can lead to much improved agreement with measurement. There are a number of combination rule methods that have been proposed to determine heteronuclear potential parameters on the basis of homonuclear parameters of Lennard-Jones potential ([42,43] and references therein). Using the different combination rules leads to some differences in the derived  $\epsilon_{ij}$  values greater than 1900% with many values different by several hundred percent and differences in the derived  $\sigma_{ij}$  values greater than 35% ( $\epsilon_{ij}$  and  $\sigma_{ij}$  are the Lennard-Jones (6–12) parameters for the atomic pairs, indices  $i$  and  $j$  here designate for atoms of active and perturbing molecule respectively). It has been found that a reliable, though time consuming, method to adjust the atom-atom parameters is to choose extremely reliable measurements for the collision system in question and adjust the intermolecular potential to reproduce these values. Applying this method has resulted in MCRB calculations showing agreement with measurement to  $\sim 0.2\%$  difference and  $\sim 2\%$  standard deviation for CO<sub>2</sub> [44–46] and  $\sim 0.2\%$  difference and  $\sim 5\%$  standard deviation for H<sub>2</sub>O [33,34].

The collision systems studied are H<sub>2</sub>O-H<sub>2</sub>O, H<sub>2</sub>O-N<sub>2</sub>, H<sub>2</sub>O-O<sub>2</sub>, and from the H<sub>2</sub>O-N<sub>2</sub> and H<sub>2</sub>O-O<sub>2</sub> results the data for H<sub>2</sub>O-air are determined. For the calculations, the atom-atom expansion is mapped from the atom-atom distances  $r_{ij}$  to the center of mass separation,  $R$ , using the expansion of Sack [47]. The expansion was carried out to 20th order and rank 4, 4 for the H<sub>2</sub>O-N<sub>2</sub> and H<sub>2</sub>O-O<sub>2</sub> collision systems (see [44] for details on this expansion) and to 8th order and rank 2, 2 for the H<sub>2</sub>O-H<sub>2</sub>O collision system. The parameters describing the electrostatic, induction, and London dispersion potentials (dipole moment, quadrupole moments, polarizabilities and ionization potentials) are given in Table 2.

**Table 2**

The molecular parameters used in the MCRB calculations.

Molecule	Parameter	Reference
H <sub>2</sub> O	$\mu = 1.85 \times 10^{-18}$ esu	[39]
	$Q_{xx} = -0.13 \times 10^{-26}$ esu	[48]
	$Q_{yy} = -2.50 \times 10^{-26}$ esu	
	$Q_{zz} = 2.63 \times 10^{-26}$ esu	
	$I_p = 12.6$ eV	[49]
	$Q_{zz} = -1.4 \times 10^{-26}$ esu	[50]
N <sub>2</sub>	$\alpha = 17.4 \times 10^{-25}$ cm <sup>3</sup>	[51]
	$I_p = 15.576$ eV	[52]
	$Q_{zz} = -1.4 \times 10^{-26}$ esu	[53]
O <sub>2</sub>	$\alpha = 18.8 \times 10^{-25}$ cm <sup>3</sup>	[51]
	$I_p = 12.063$ eV	[49]

**Table 3**

Measured parameters of the 183- and 380-GHz lines of the H<sub>2</sub>O molecule at 296 K used for the potential adjustments.

Parameter, MHz/Torr	O <sub>2</sub>		N <sub>2</sub>	
	183	380	183	380
$\gamma$	2.610(11)	2.403(24)	4.288(16)	4.206(25)
$\delta$	-0.093(4)	-0.081(1)	-0.090(2)	-0.104(1)

**Table 4**

MCRB Half-widths and line shifts in MHz/Torr for 183-GHz transition self- and air-broadened at the 13 temperatures of the study.

T(K)	H <sub>2</sub> O-H <sub>2</sub> O		H <sub>2</sub> O-air	
	$\gamma$	$\delta$	$\gamma$	$\delta$
200	26.98	-3.210	5.453	-0.2104
225	24.39	-2.348	4.962	-0.1969
275	20.57	-1.221	4.240	-0.1465
296	19.34	-0.905	4.007	-0.1303
350	16.81	-0.3510	3.528	-0.0989
500	12.51	0.2481	2.704	-0.0554
700	9.509	0.3983	2.110	-0.0359
1000	7.144	0.3836	1.625	-0.0264
1250	5.986	0.3432	1.380	-0.0226
1500	5.181	0.3050	1.206	-0.0198
2000	4.126	0.2446	0.9734	-0.0155
2500	3.467	0.2017	0.8262	-0.0123
3000	3.021	0.1704	0.7253	-0.0099

In the calculations, the reduced matrix elements for the collisionally induced transitions were determined using ab initio wavefunctions as described in Lamouroux et al. [36].

Generally, the atom-atom part of the intermolecular potential needs to be adjusted to obtain very good agreement with measurement. Beginning with the combination rules of Hirschfelder et al. [54] the starting atom-atom parameters are determined (called potential 0 or *pot00*) and the potential is adjusted to reproduce high quality measured values. For the H<sub>2</sub>O-N<sub>2</sub> collision system the potential of Vispoel et al. [34] *pot24* was taken for the MCRB calculations. For the H<sub>2</sub>O-O<sub>2</sub> collision system, calculations began using the *pot00* potential and the atom-atom coefficients adjusted to reproduce results for the 183- and 380-GHz water lines (Table 3) reported in Koshelev et al. [55], which are in a good agreement with previous measurements [56,57] but have smaller uncertainty.

The final potential was *pot89*. For the H<sub>2</sub>O-H<sub>2</sub>O collision system the effect of the atom-atom potential is weak (this collision system has a strong electrostatic component that dominates) so the *pot00* potential was chosen.

Once the potentials were chosen for each collision system, calculations for the line under consideration can be made at any temperature. The MCRB calculations were made for 13 temperatures between 200 and 3000 K. These data are presented in Table 4.

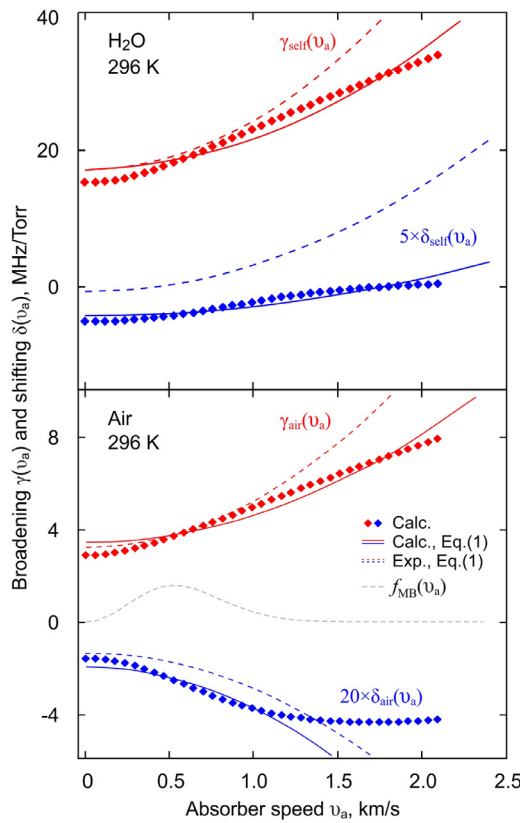


**Fig. 4.** Speed-dependence of the 183-GHz line broadening (shown by red color) and shifting (blue color) parameters in pure water vapor (upper panel) and air (lower panel). Results of MCRB calculations (symbols) and their approximation by the quadratic function Eq. (1) (solid curves) are given in comparison with corresponding dependencies derived from experimental data (red and blue dashed curves). All line-shifting data are multiplied by 5 and 20 for pure water and air, respectively. Dashed grey curve in the lower panel is the Maxwell distribution of  $\text{H}_2\text{O}$  molecule speeds in arbitrary units.

From these data the temperature dependence of the half-width and line shift can be determined.

#### 4.2. Calculated speed-dependence of the collisional parameters

The speed-dependence of the half-width and line shift in the Hartman-Tran profile is given by quadratic speed-dependence [28,29] model (Eq. (1)). The MCRB calculations can be used to predict the speed-dependences of the collision parameters.

The collisional cross-sections were evaluated at 35 relative velocity values approximately from 400 to 8000 m/s. The broadening and shifting versus the speed of the active molecule were then obtained from a Maxwell-Boltzmann average over the perturber velocity [18,58–61]

$$\gamma(v) + i\delta(v) = \frac{1}{\tilde{v}} \frac{2}{\sqrt{\pi}} \int_0^\infty dv_{rel} [\gamma(v_{rel}) + i\delta(v_{rel})] \frac{v_{rel}}{v} \sinh \left[ \frac{2vv_{rel}}{\tilde{v}^2} \right] e^{-\frac{v^2+v_{rel}^2}{\tilde{v}^2}} \quad (4)$$

where  $\tilde{v}$  is the most probable speed of perturber molecule. Obtained values of  $\gamma(v)$  and  $\delta(v)$  (recall that  $\gamma(v) = \Gamma(v)/P$  and  $\delta(v) = \Delta(v)/P$ ) are used for fits of Eq. (1) to determine  $\gamma_0$ ,  $\gamma_2$ ,  $\delta_0$ , and  $\delta_2$ . A least-squares fitting procedure was employed, weighted by the Maxwell-Boltzmann distribution of speeds. Results for 296 K are shown in Fig. 4 as typical example. From these data, the temperature dependence of SD parameters can be determined.

## 5. Temperature dependence of line parameters

### 5.1. Modeling

A rigorous derivation of the temperature dependence of the half-width and the line shift, even if the latter changes sign, was suggested by Gamache and Vispoel [62]

$$\Gamma(T) + i\Delta(T) = \sum_{k=1}^{N_k} c_k \tilde{T}^{n_k} + i \sum_{l=1}^{N_l} d_l \tilde{T}^{q_l} \quad (5)$$

where  $\tilde{T}$  is a unitless temperature given in terms of a reference temperature,  $\tilde{T} = T_{ref}/T$ ,  $N_k$  and  $N_l$  are the number of terms in the power series used to fit the collisional cross-sections. In practice it is found that only two terms are necessary to fit the half-width and line shift over large temperature ranges (thousands of Kelvin) yielding what has been termed the double power law (DPL) expressions

$$\Gamma(T) = c_1 \tilde{T}^{n_1} + c_2 \tilde{T}^{n_2} \quad (6)$$

and

$$\Delta(T) = d_1 \tilde{T}^{q_1} + d_2 \tilde{T}^{q_2} \quad (7)$$

This model has been adopted by the HITRAN database [63]. However, it will be some time before the entire database will be populated with the DPL parameters.

What has been used to date is the standard power law (PL)

$$X(T) = X(T_{ref}) \left( \frac{T_{ref}}{T} \right)^{n_X}, \quad (8)$$

where  $X$  is the modeled parameter,  $T_{ref}$  is usually taken as the HITRAN reference of 296 K, and  $n_X$  is the temperature exponent. Note that  $n_X$  is the only one empirical parameter of the model (8) to describe the temperature dependence. In case of pressure-broadening,  $\gamma$  for VP and  $\gamma_0$  for qSDVP, the power law has been widely used in experimental and theoretical studies and in spectroscopic databases. In most cases corresponding to narrow temperature intervals (up to 50–100 K), the power law demonstrates good agreement with the experimental data, but the value of  $n_\gamma$  can depend on the temperature range used for the data analysis and the extrapolation properties of the power law can be rather poor (see [62] for details).

The situation is more ambiguous for the temperature dependence of the pressure shift. Similar to pressure broadening, the power law can be used for the line-shift parameter,  $\delta$  for VP or  $\delta_0$  for qSDVP, in narrow temperature intervals if the line shift does not change sign. To estimate  $n_\delta$ , Pickett [58] derived the following relation between the shifting and broadening PL temperature exponents:

$$n_\delta = 1.5n_\gamma + 0.25 \quad (9)$$

The change of the sign of the pressure shift with temperature was predicted by theory [62,64] and observed in experiments [65,66]. In such cases PL is not applicable. To solve this problem, Frost [64] suggested the more complicated formula (two empirical parameters):

$$\delta(T) = \delta' \cdot \left[ \frac{T_{ref}}{T} \right]^{n'_\delta} \cdot \left( 1 + A \cdot \ln \left( \frac{T}{T_{ref}} \right) \right), \quad (10)$$

where  $\delta' = \delta(T_{ref})$ ,  $n'_\delta$  and  $A$  are adjustable parameters. When  $A = 0$ , Frost's formula becomes the power law. Several experimental studies, e.g., Smith et al. [67], Wilzewski et al. [68] demonstrated a linear dependence:

$$\delta(T) = \delta' + \delta'' \cdot (T - T_{ref}) \quad (11)$$

and, rarely, a quadratic polynomial behavior [65]:

$$\delta(T) = \delta' + \delta'' \cdot (T - T_{ref}) + \delta''' \cdot (T - T_{ref})^2 \quad (12)$$

**Table 5**

Fitted empirical coefficients of model functions, describing temperature dependence of the line shape parameters of the 183-GHz water line relative to  $T_{ref} = 296$  K for the regular Voigt profile. Errors in parenthesis are the fit uncertainties. Parameters in bold are the ones recommended for their use in radiative transfer modeling.

Line shape parameter	Fitted coefficients		H <sub>2</sub> O		Air	
	Coeff.	Units	Meas.	Calc.	Meas.	Calc.
$\gamma$	Eq. (8)	$\gamma'$	MHz/Torr	<b>19.746(22)</b>	19.336	<b>3.945(6)</b>
		$n_\gamma$	unitless	<b>0.831(9)</b>	0.823	<b>0.632(11)</b>
	Eq. (6)	$c_1$	MHz/Torr	–	15.53	–
		$n_1$	unitless	–	0.7384	–
		$c_2$	MHz/Torr	–	3.802	–
		$n_2$	unitless	–	1.260	–
$\delta$	Eq. (10)	$\delta'$	MHz/Torr	<b>0.145(7)</b>	-1.272	<b>-0.0965(10)</b>
		$n'_\delta$	unitless	<b>1.25(22)</b>	1.219	<b>1.850(73)</b>
		$A$	unitless	<b>17.26(96)</b>	-1.458	<b>0*</b>
	Eq. (7)	$d_1$	MHz/Torr	–	-85.33	–
		$q_1$	unitless	–	1.428	–
		$d_2$	MHz/Torr	–	84.44	–
		$q_2$	unitless	–	1.398	–

\* Coefficients were fixed to zero value in the fit.

**Table 6**

Same as **Table 5** but for the speed-dependent Voigt profile.

Line shape parameter	Fitted coefficients		H <sub>2</sub> O		Air	
	Coeff.	Units	Meas.	Calc.	Meas.	Calc.
$\gamma_0$	Eq. (8)	$\gamma'_0$	MHz/Torr	<b>20.013(19)</b>	18.812	<b>4.044(7)</b>
		$n_{\gamma_0}$	unitless	<b>0.821(8)</b>	0.788	<b>0.617(11)</b>
	Eq. (6)	$c_1$	MHz/Torr	–	18.955	–
		$n_1$	unitless	–	0.800	–
		$c_2$	MHz/Torr	–	-0.059	–
		$n_2$	unitless	–	5.18	–
$\gamma_2$	Eq. (8)	$\gamma'_2$	MHz/Torr	<b>1.946(23)</b>	1.9216	<b>0.543(4)</b>
		$n_{\gamma_2}$	unitless	<b>0.571(95)</b>	0.8241	<b>0.412(55)</b>
	Eq. (6)	$c_1$	MHz/Torr	–	1.923	–
		$n_1$	unitless	–	0.8251	–
		$c_2$	MHz/Torr	–	-0.001	–
		$n_2$	unitless	–	3.22	–
$\delta_0$	Eq. (10)	$\delta'_0$	MHz/Torr	<b>0.181(16)</b>	-0.785	<b>-0.099(2)</b>
		$n_{\delta_0}$	unitless	<b>0.98(44)</b>	1.368	<b>1.82(12)</b>
		$A$	unitless	<b>12.57(121)</b>	-3.035	<b>0*</b>
	Eq. (7)	$d_1$	MHz/Torr	–	-11.57	–
		$q_1$	unitless	–	1.48	–
		$d_2$	MHz/Torr	–	10.79	–
$\delta_2$	Eq. (8)	$\delta'_2$	MHz/Torr	<b>0.21(11)**</b>	0.130**	<b>-0.021(38)**</b>
		$n_{\delta_2}$	unitless	<b>0</b>	0	<b>0</b>
		$d_1$	MHz/Torr	–	-0.190	–
	Eq. (7)	$q_1$	unitless	–	2.72	–
		$d_2$	MHz/Torr	–	0.335	–
		$q_2$	unitless	–	1.67	–

\* Coefficients were fixed to zero value in the fit.

\*\* Mean value within experimental temperature range.

of the pressure shift on temperature. Here  $\delta' = \delta(T_{ref})$ ,  $\delta''$  and  $\delta'''$  are two adjustable empirical parameters. Note that the double power law (Eqs. (6) and (7)) employs four adjustable (and strongly correlated) parameters.

The HITRAN database [63] currently uses the power law (8) for the line broadening and the linear law (11) for the line shifting, although there are few values on the database using the linear law.

Concerning the temperature dependence of the SD parameters  $\gamma_2$  and  $\delta_2$ , the power law was used in several studies (e.g., Wilzewski et al. [68], Cich et al. [69], Goldenstein and Hanson [70]) and it was found to be well suited within the experimental uncertainties to measured  $\gamma_2$  but not always to  $\delta_2$  [69]. Recent work [71] shows that the DPL gives a better representation of the temperature dependence of the SD parameters.

The operating temperature range of our experimental data is too narrow for unambiguous determination of the DPL parameters. Moreover, the spread of experimental values for  $\gamma_2$  and  $\delta_2$  makes this task meaningless. So we use the DPL representation only for

the theoretical data. The latter allows us to demonstrate the expected temperature dependence of the line shape parameters in a much wider range than is available for experimental studies.

## 5.2. Experimental and theoretical results

**Tables 5** and **6** contain the coefficients of Eqs. (6)–(12) fitted to the experimental and calculated temperature dependencies of the line shape parameters for the self- and air-broadened 183-GHz water line for regular- and speed dependent Voigt profiles, respectively. Data obtained on the line broadening and shifting are discussed in comparison with each other and with previously known data in the two following subsections.

### Pressure-broadening

Self- and air-broadening parameters of the 183-GHz line obtained from the fit of the Voigt profile to observed spectra and

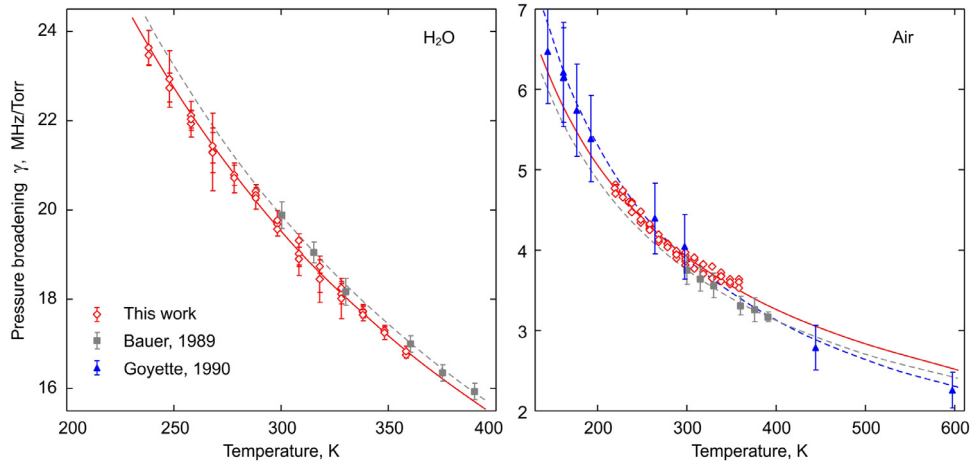


**Fig. 5.** Temperature dependence of the self-broadening (left panel) and air-broadening (right panel) parameters of the 183-GHz line. Three experimental datasets derived from the fitting of the Voigt profile are shown: data of the present study (red diamonds), data from [72] (gray squares) and from [73] (blue triangles). PL functions fitted to these datasets separately are shown by red solid, grey dashed and blue dashed curves, respectively. Error bars for the present data and data from [72] correspond to  $\pm 3\sigma$  uncertainty determined from the line shape fitting and 10% quoted uncertainty is plotted for data from [73]. Error bars for the present air-broadening data are comparable with the symbol size.

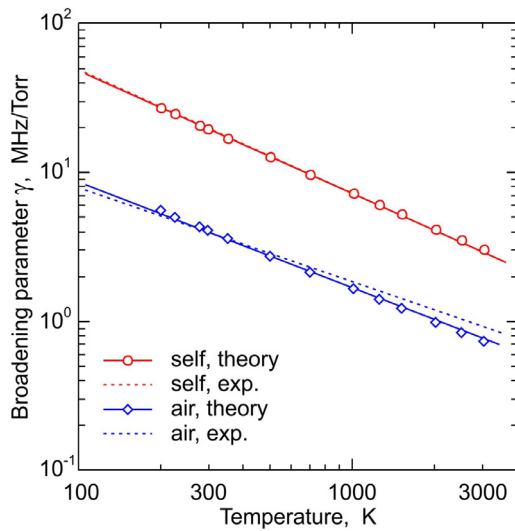


**Fig. 6.** Measured and calculated temperature dependence of pressure broadening for H<sub>2</sub>O-H<sub>2</sub>O (upper part, red color) and H<sub>2</sub>O-air (lower part, blue color). Shown are the calculated values (symbols) and the power-law fits (solid and dotted lines for measured and calculated data, respectively).

approximated by the power law function (8) are shown in Fig. 5 in comparison with previously reported experimental data [72,73]. Fig. 6 compares the measured and calculated parameters of this study in a broad temperature range. The relative difference between MCRB and measured  $\gamma(296)$  is 1.6 and 2.1 % for air- and self- broadening, respectively.

Table 7 presents a comparison of the 183-GHz line pressure-broadening parameters and their temperature behavior with the earlier experimental studies [56,72–74]. One should note that only VP values are available in the literature and have been considered for comparison. Experimental data from the paper of Bauer et al. [72] for both perturbers demonstrate some difference from our results (Fig. 5). In the case of self-broadening, the value of  $\gamma_{self}(296)$  from [72] is almost 2% higher than our result, but the temperature exponent  $n_{\gamma_{self}}$  is in agreement with our value within experimental uncertainties. For air-broadening the situation is the opposite: our value of  $\gamma_{air}(296)$  is more than 4% higher than that from [72]; however, the temperature exponents  $n_{\gamma_{air}}$  are again in

agreement. However, for both self- and air-broadening parameters, our results and those of [72] can be considered consistent within the three-fold quoted uncertainties. Another experimental  $n_{\gamma}$ , obtained by Goyette and De Lucia [73] from data in the wide temperature range 144–597 K, is about 20% higher than our value, while  $\gamma_{air}(296)$  coincides with our value within the experimental errors. The discrepancy between the pressure broadening parameters and temperature exponents obtained in different studies can only be explained by unknown systematic errors of the techniques and methods of measurement.

The temperature exponent,  $n_{\gamma_{air}}$ , from the PL fit to the MCRB calculations is 0.750 compared with the value of 0.632 from the measurements presented here. The theoretical value is closer to those of Goyette et al [73] and Payne et al [74]. For self-broadening the theoretical value of  $n_{\gamma_{self}}$  is 0.823, less than 1% smaller than measured in the present work. Note that the DPL and PL fit results for the calculated half-width coincide with each other in Fig. 6 up to the thickness of the line, suggesting that the power law is suitable for the 183-GHz line pressure broadening in a broad temperature range.

A comprehensive compilation of the  $\gamma_{air}(296)$  and  $\gamma_{self}(296)$  of the 183-GHz water line according to the results of various studies is presented in Tretyakov [14]. To avoid repetition of this analysis we compare our results only with the best estimated values  $\gamma_{air}(296) = 3.926(20)$  MHz/Torr and  $\gamma_{self}(296) = 19.7(5)$  MHz/Torr (see [14] for details). Our values in Table 7 are in excellent agreement with the values recommended in Tretyakov [14], indicating the reliability of our present results.

#### Pressure-shift

Temperature dependence of the measured self- and air-shift parameters of the 183-GHz water line are presented in Fig. 7. It was found for the first time that the self-shift parameter of the line changes sign at about 280 K from negative to positive as temperature increases. The air-shift remains negative in the studied temperature range.

The measured and MCRB calculated values of the line shift can be compared in Fig. 8. It is remarkable that the theoretical and experimental data demonstrate similar temperature dependence for both perturbers. The calculated self-shift also changes its sign but at a somewhat higher temperature of about 420 K. Comparing the measured and MCRB  $\delta(296)$  values gives differences of  $-0.034$  and  $-1.05$  MHz/Torr for air- and self- broadening respectively, which

**Table 7**

Comparison of the measured self- and air-broadening parameters,  $\gamma_{self}$ (296) and  $\gamma_{air}$ (296), and their PL temperature exponents  $n_{\gamma_{self}}$  and  $n_{\gamma_{air}}$  with earlier results.

Parameter	This study	Previous study	Difference	
			Absolute <sup>a</sup>	Relative <sup>b</sup>
$\gamma_{self}$ (296), MHz/Torr	19.746(22)	20.11(8) [72] 19.72(4) <sup>c</sup> [56]	-0.364 0.026	-1.8 0.13
$n_{\gamma_{self}}$	0.831(9)	0.85(5) [72] 3.78(6) [72] 3.815(7) <sup>c,d</sup> [56] 3.93(14) [73] 3.99 [74]	-0.019 0.165 0.130 0.015 -0.045	-2.3 4.1 3.3 0.4 -1.1
$\gamma_{air}$ (296), MHz/Torr	3.945(6)	0.64(10) [72] 0.76(3) [73] 0.769 [74]	-0.008 -0.128 -0.137	-1.3 -20.2 -21.7
$n_{\gamma_{air}}$	0.632			

<sup>a</sup> Absolute difference was calculated as (This study - Previous study).

<sup>b</sup> Relative difference in % was calculated as ((This study - Previous study)/This study)·100.

<sup>c</sup> Recalculated to 296 K using power law and coefficients from Table 5.

<sup>d</sup> Calculated as  $\gamma_{air} = 0.78\gamma_{N_2} + 0.21\gamma_{O_2} + 0.01\gamma_{Ar}$ .

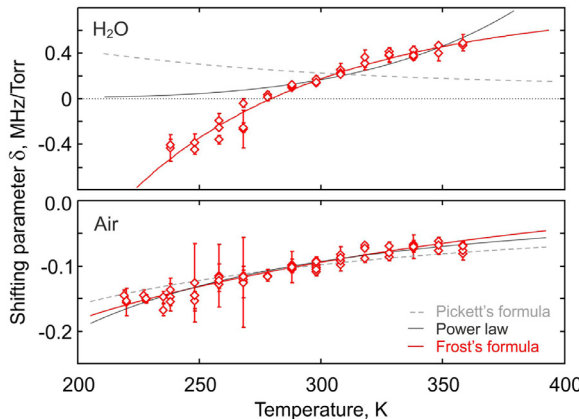


**Fig. 7.** Measured temperature dependence of the self-shift (upper panel) and air-shift (lower panel) parameters of the 183-GHz line obtained from fitting the Voigt profile. Experimental data of the present study are shown by diamonds. Solid red lines are results of the fit of Frost's formula (10) to the data; solid black and dashed grey lines demonstrate the power law with  $n_{\delta}$  fitted and calculated by means of Pickett's formula (9), respectively. Error bars correspond to  $\pm 3\sigma$  uncertainty determined from the line-shape fitting.

can be considered good agreement (especially for air- broadening) taking into account the smallness of the effect and the complexity of the line shifting phenomenon for theoretical calculations.

The data on the self-shift cannot be reproduced by the power law Eq. (8) with the use of  $n_{\delta_{self}}$  either calculated by Pickett's formula (9) from the experimental  $n_{\gamma_{self}}$  or fitted. Frost's formula (10) fits well the experimental dependences (Fig. 8). Moreover, for the self-shift both formulae demonstrate reasonable extrapolation ability beyond the range of measurements (Fig. 8, upper panel).

Our data on measured self-shift validate both of the experimental results known from the literature. The first one was obtained by Bauer et al. [72] in the temperature range 300–390 K. Where (we quote) “attempts were made to measure the very small pressure-shift of the 183 GHz pure water vapor line. The line-shift was determined to be positive and smaller than +0.7 MHz/Torr.” The second value of +0.23(3) MHz/Torr reported by Golubiatnikov [56] for 300 K (and used as the suggested value in Tretyakov [14]) agrees with our data within  $2\sigma$ .

In contrast with the self-shift, the relationships (8)–(12) reproduce well the observed air-shifting temperature dependence, with comparable accuracy. The difference between the fit qual-

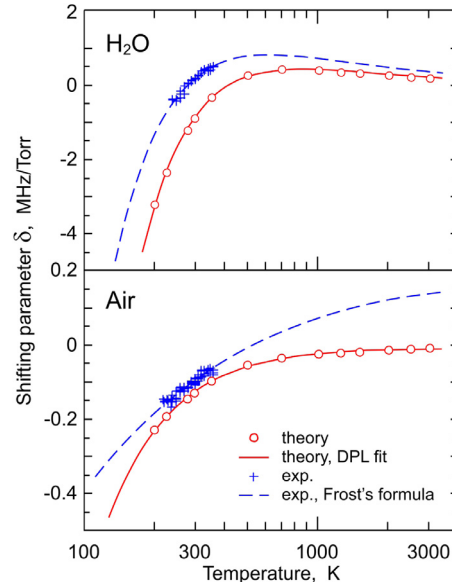


**Fig. 8.** Broad band temperature dependence of the 183-GHz line shifts for  $H_2O$ - $H_2O$  (upper panel) and  $H_2O$ -air (lower panel). Shown are the measured (blue crosses) and the calculated (red circles) values, the double power law fits (red solid curves) for calculated data, and Eq. (10) fits (blue dashed lines) for experimental data.

ity (standard deviation of exp.-calc.) of the worst and the best fitted models is only 35%. Note that the power law with the temperature exponent  $n_{\delta_{air}} = 1.2$ , calculated by means of Pickett's formula (9) from the experimental  $n_{\gamma_{air}}$ , and fitted  $\delta_{air}(296) = -0.100(1)$  MHz/Torr suits the experimental points on the temperature dependence of the air-shift. Frost's formula demonstrated the best fit quality.

An excellent agreement can be noted between the air-pressure shift values measured in this work and suggested in Tretyakov [14] ( $-0.0965(10)$  vs.  $-0.096(10)$  MHz/Torr, respectively) on the basis of the data from [56].

#### Speed-dependence of pressure-broadening and pressure-shift

The SD broadening  $\gamma_0(T)$  and shifting  $\delta_0(T)$  should be only slightly different from  $\gamma(T)$  and  $\delta(T)$  because of relative weakness of the effect. Indeed, the measured  $\gamma_0$  (as expected from previous experimental studies) is higher than  $\gamma$  by about 1.3%

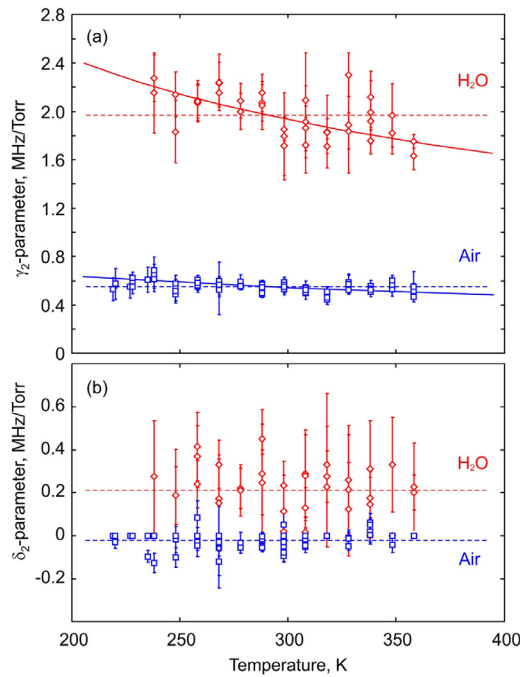


**Fig. 9.** Temperature dependence of the speed-dependent broadening  $\gamma_2$  (a) and shifting  $\delta_2$  (b) for self-broadening (red diamonds) and air-broadening (blue squares) of the 183-GHz line. Solid lines are results of the power law fit. Dashed lines indicate mean values of the corresponding parameters.

for self-broadening and 1.5% for air-broadening. Their temperature exponents coincide within the experimental uncertainties. The corresponding differences between MCRB values are  $-2.3$  and  $-3\%$  for self- and air-broadening, respectively. (The opposite sign of the difference is probably related to the fact that  $\gamma$  calculated by Eq. (2) is for molecules moving with the mean relative thermal velocity, whereas  $\gamma$  obtained from fitting the Voigt profile to the observed spectrum is just an *ad hoc* parameter, which inherently takes into account the velocity distribution.) The calculated value of  $n_{\gamma_0}$  is smaller than  $n_\gamma$  by about 4.5% for both perturbers. The measured  $\delta_0$  values are also somewhat higher than  $\delta$  for both perturbers, although these parameters as well as their temperature dependences coincide with each other within one and two  $\sigma$  for air- and self-broadening, respectively. The calculated values of  $\delta_0$  have slightly faster temperature dependence and are smaller than  $\delta$  by about 1.6 and 38% for air- and self-pressure broadening respectively. We believe that such different behavior of the line shift from the measured data is due to the same reason mentioned above for the line broadening.

The measured dependencies of the speed-dependent broadening  $\gamma_2$  and shifting  $\delta_2$  parameters versus temperature are shown in Fig. 9. It might be expected [75,76] that  $\gamma_2$  has the same temperature dependence as speed-averaged broadening  $\gamma_0$ . However, the PL function (8) fitted to our results demonstrates that  $n_{\gamma_2}$  is almost 30% smaller than  $n_{\gamma_0}$  for both self- and air-broadening, which is in general agreement with other studies (e.g., [68]). The mean temperature-independent values  $\gamma_{2\text{self}}^{\text{mean}} = 1.97(18)$  MHz/Torr and  $\gamma_{2\text{air}}^{\text{mean}} = 0.551(43)$  MHz/Torr can be used as a less-accurate experimental estimate of the SD effect.

For SD shifts  $\delta_{2\text{self}}$  and  $\delta_{2\text{air}}$ , only mean values can be determined from the experimental data (Table 6), and used for modeling the SD effect within the temperature interval under consideration.

The SD parameters  $\gamma_2$  and  $\delta_2$ , calculated in a broad temperature range, are shown in Fig. 10 in comparison with the discussed

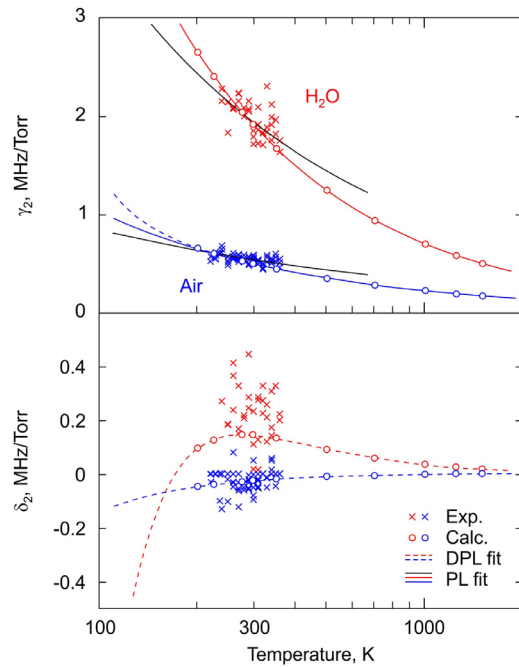


**Fig. 10.** Measured (crosses) and calculated (circles) parameters of the speed-dependence,  $\gamma_2$  (top panel) and  $\delta_2$  (bottom panel) for the 183-GHz line in air (blue color) and in water vapor (red color) versus temperature. The power-law and the double-power-law fits are shown by solid and dashed curves, respectively. Fits of PL to experimental data are shown in black for clarity.

experimental data. The agreement between calculated and measured data within experimental uncertainty is prominent. Calculations show that  $n_{\gamma_2}$  is very close to  $n_{\gamma_0}$  for both self- and air-broadening. The same can be stated for  $n_{\delta_2}$  in the case of air-pressure shifting. For the self-shifting the temperature dependence of  $\delta_2$  is more complicated. The DPL model fits the calculated data better than the PL model but it is certainly ambiguous for fitting noisy experimental data (Fig. 10).

In spite of some difference between the measured and calculated values, we believe that good general agreement between measured and calculated SD parameters can be stated, taking into account the smallness of the SD effect, the complexity of its theoretical calculation and imperfection of its representation by the quadratic model (Fig. 4). Bearing in mind deviation between MCRB and measured line shift values and taking into account known difficulties in calculating this effect we would like to emphasize the importance of accurate laboratory measurements of this parameter for atmospheric applications.

## 6. Impact on radiative transfer modeling and water vapor retrievals

This section reports the impact of the updated spectroscopic parameter values on radiative-transfer calculations and atmospheric water-vapor retrievals. In fact, line shape and the associated spectroscopic parameters are at the core of atmospheric-absorption and radiative-transfer models. Radiative-transfer models are extensively used to simulate passive remote-sensing observations. Simulations are used for a variety of applications, including the validation of real observations and the solution of the inverse problem, i.e., the retrieval of atmospheric variables from radiometric observations. In particular, the shape and the associated spectroscopic parameters of the 183-GHz water-vapor line affect the simulated radiometric observations in a wide frequency range and consequently the retrievals of atmospheric water-vapor profiles requiring radiative-transfer calculations. In the following,

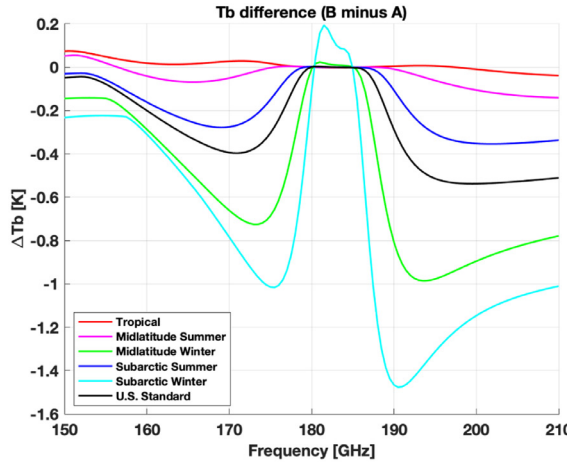


**Fig. 11.** Difference between simulated bottom-of-atmosphere vertically-downwelling  $T_b$  obtained using the VVW line shape with the parameters proposed here (Table 5) and as in Tretyakov [14]. Different colors indicate six typical atmospheric climatologies (tropical, midlatitude summer, midlatitude winter, subarctic summer, subarctic winter, US standard). Left: absolute difference  $\Delta T_b$  (K). Right: Percent difference  $\Delta T_b/T_b$  (%)

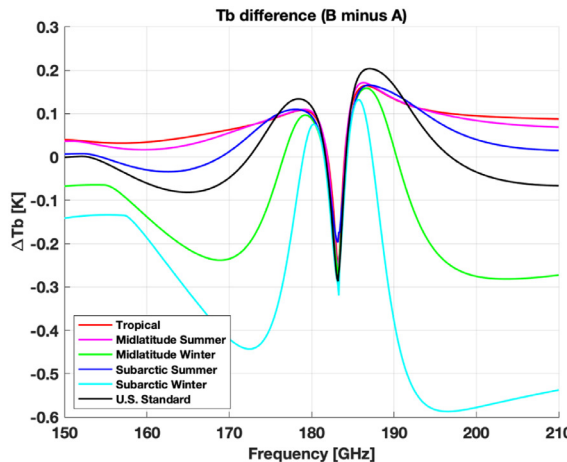
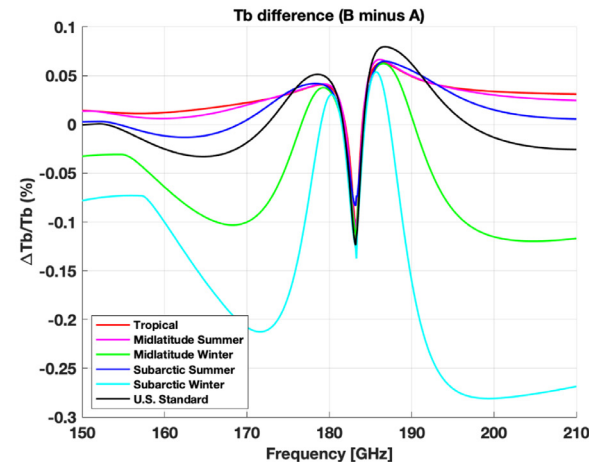
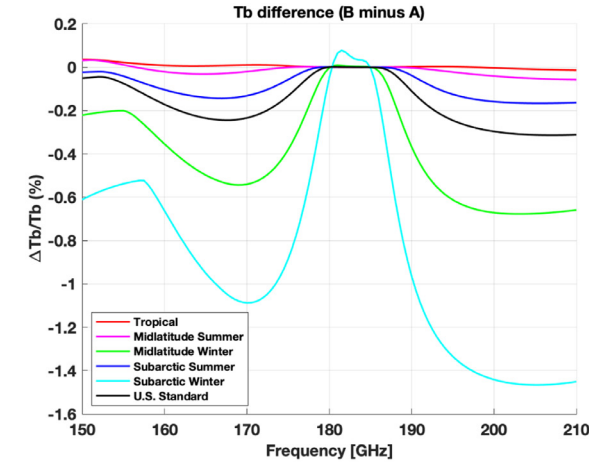


**Fig. 12.** Same as in Fig. 11 but for top-of-atmosphere upwelling  $T_b$

radiative-transfer calculations are based on the line-by-line microwave radiative-transfer routines available from [77]. Using the same radiative-transfer code, three different absorption models are implemented to quantify the impact of the parameterisation reported here:

- A) the reference implementation assumes the standard Van Vleck and Weisskopf (VVW) line shape [78] with the set of parameters given in Tretyakov [14]. Note that the VVW line shape is used instead of the Voigt profile because Doppler broadening of the line can be neglected at the relatively high pressures typical of the Earth's lower atmosphere;
- B) the updated VVW implementation assumes the same line shape as the reference, but with the set of measured parameters proposed in this work (Table 5, Voigt profile);
- C) this implementation assumes the quadratic speed-dependent VVW profile (qSDVVW) with the set of measured parameters reported in this work (Table 6, speed-dependent Voigt profile). Note that the qSDVVW includes both the positive- and negative-frequency resonances and takes into account frequency dependence of the radiation term [15], whereas qSDVP includes only the positive-frequency resonance and neglects the impact of the radiation term.



The software used in Rosenkranz and Cimini [15] was modified to incorporate Eq. (10) for the temperature dependence of line shift. We use the recommended parameter values highlighted in bold in Tables 5 and 6, except that for  $\gamma_2$ , we used the mean values shown in Fig. 9, considering that our purpose is to illustrate the approximate size of their effect. The water-vapor continuum coefficients were then readjusted to compensate for the changes in line parameters, as discussed in Cimini et al. [16].

Both up- and down-looking observing geometries are considered to address typical ground-based, airborne, and satellite applications. Fig. 11 shows bottom-of-atmosphere downwelling brightness temperature ( $T_b$ ) differences obtained processing the same atmospheric temperature and water-vapor profile with two of the absorption-model implementations, A and B (i.e. reference and updated VVW line shape parameters, respectively). The  $T_b$  difference  $\Delta T_b$  is computed for six typical atmospheric climatology conditions (tropical, midlatitude summer, midlatitude winter, subarctic summer, subarctic winter, US standard). Similarly, Fig. 12 shows top-of-atmosphere upwelling  $T_b$  differences for the same two model implementations, A and B. For both bottom-of-atmosphere and top-of-atmosphere simulations, the impact is minimum for tropical (warm and humid) conditions

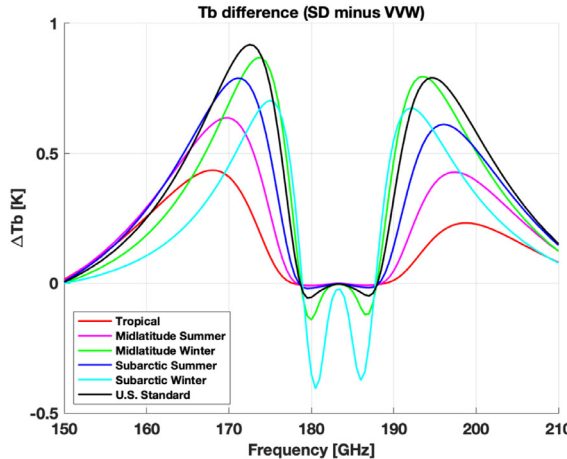


**Fig. 13.** Difference between simulated bottom-of-atmosphere downwelling  $T_b$  obtained using the qSDVVW and the VVW line shapes with the parameters proposed here (Table 5). Different colors indicate six typical atmospheric climatologies (tropical, midlatitude summer, midlatitude winter, subarctic summer, subarctic winter, US standard). Left: absolute difference  $\Delta T_b$  (K). Percent difference  $\Delta T_b/T_b$  (%).

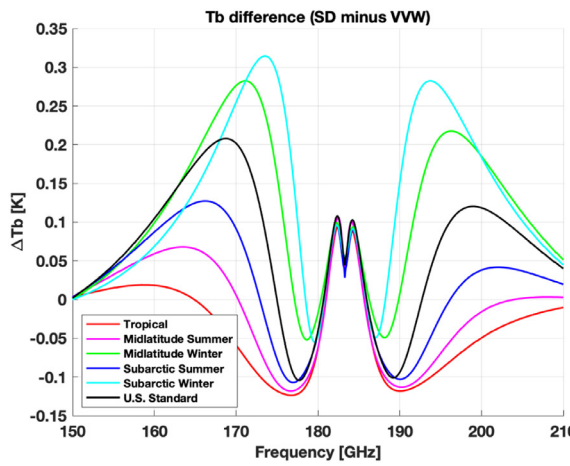


**Fig. 14.** Same as in Fig. 13 but for top-of-atmosphere upwelling  $T_b$ .

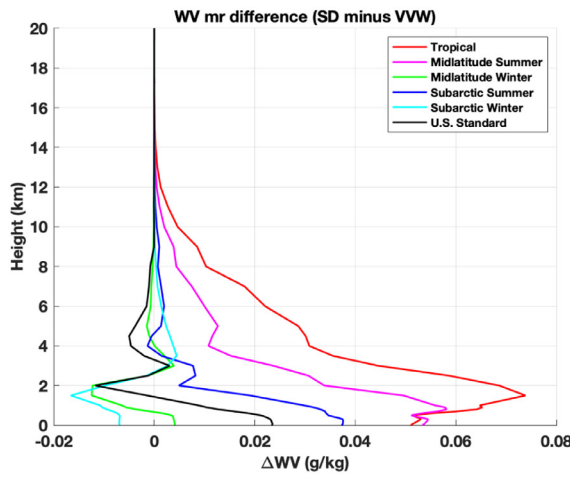
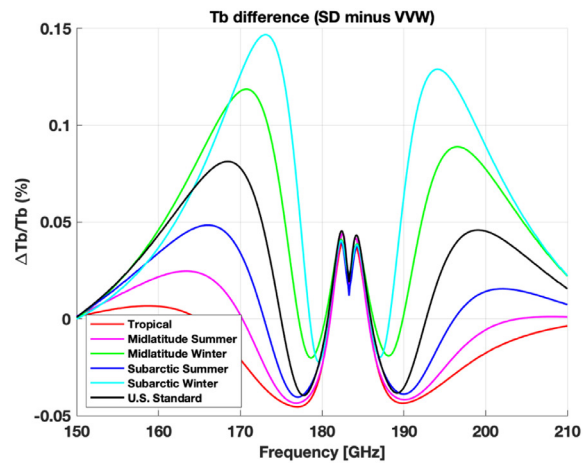


**Fig. 15.** Water vapor mixing ratio retrieval impact of qSDVVW vs. VVW for downwelling  $T_b$  around 183 GHz. Left:  $\Delta WV$  (g/kg). Right:  $\Delta WV/WV$  (%).

and maximum for subarctic winter (cold and dry) conditions. The maximum impact is reached around 195 GHz,  $\sim 1.8\%$  for bottom-of-atmosphere  $T_b$ , while  $< 0.4\%$  for top-of-atmosphere  $T_b$ .

The effect of the qSDVVW with respect to the VVW (with parameters as in Table 5, i.e. implementation C minus implemen-

tation B) is shown in Figs. 13 and 14, respectively for bottom-of-atmosphere downwelling and top-of-atmosphere upwelling  $T_b$ . Here,  $T_b$  differences are nearly symmetrical with respect to the line center. Again, the impact is minimum for tropical and maximum for subarctic winter conditions. The maximum impact is reached

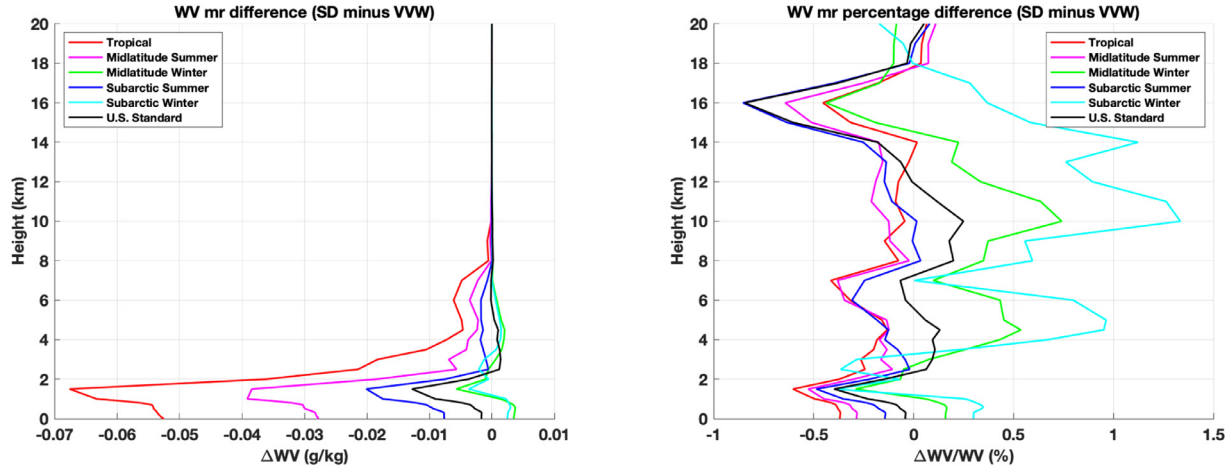


**Fig. 16.** Water vapor mixing ratio retrieval impact of qSDVVW vs VVW for upwelling  $T_b$  around 183 GHz (assuming 0.6 surface background emissivity). Left:  $\Delta \text{WV}$  (g/kg). Right:  $\Delta \text{WV}/\text{WV}$  (%).

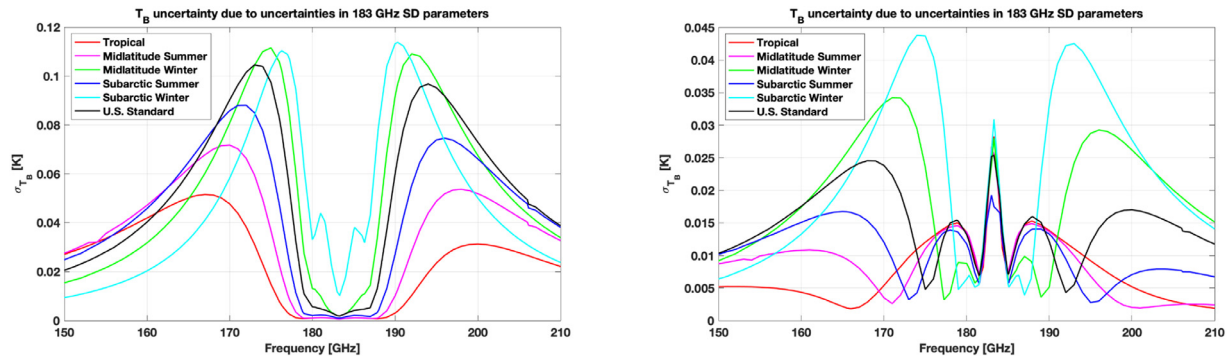


**Fig. 17.**  $T_b$  uncertainty ( $\sigma(T_b)$ ) due to the uncertainty in 183-GHz line SD parameters. Six climatological atmospheric conditions (color-coded) have been used to compute  $K_p$ . Left: Vertically downwelling  $T_b$ . Right: Vertically upwelling  $T_b$ .

around 172 and 193 GHz,  $\sim 0.6\%$  for bottom-of-atmosphere  $T_b$ , while  $< 0.14\%$  for top-of-atmosphere  $T_b$ .

To quantify the impact of line model and updated parameterisation on atmospheric water vapor retrievals, a simple inverse method is implemented here, exploiting linear regression. The method is similar to that used in Rosenkranz and Cimini [15] and Cimini et al. [16]. A dataset of diverse atmospheric profiles [79,80] is processed to produce simulated  $T_b$  (using B, i.e. VVW line shape with Voigt profile parameters from Table 5) at channels typically exploited for water vapor retrievals from ground-based (GVRP [2,81]) and satellite (ATMS [82,83]) observations. The water vapor profiles from the diverse dataset and the corresponding simulated  $T_b$  are used to train the regression coefficients. Water vapor profiles are then retrieved by feeding the regression matrix with the  $T_b$  simulated with either implementation B (VVW) or C (qSDVVW). The difference between the water profiles retrieved from B and C shows the impact of qSDVVW versus VVW on water vapor retrievals, i.e. the additional error one would have to accept when neglecting the speed-dependent effect on line shape.

Such an impact is shown in Figs. 15 and 16 for ground-based and satellite-based retrievals, respectively. Percentage differences are up to 2.0% for ground-based retrievals, while up to 1.5% for satellite retrievals. These percentages are larger than the percentage change in  $T_b$ , which reflects amplification of relative error as a consequence of reconstruction of the vertical profile from the spectrum. Note that the sign depends on climatology and viewing geometry: the difference in warmer/moister environments tends to be positive for the ground-based retrievals while negative for

satellite retrievals. The opposite seems true for colder/drier environments, although less clear.

The uncertainty of the measured spectroscopic parameters reported in Table 6 can be propagated through the radiative-transfer calculations, following the approach described in Cimini et al. [16]. The full covariance matrix has been estimated in order to take into account the correlation between spectroscopic parameters. Calling  $K_p$  the Jacobian of the radiative transfer model with respect to each parameter (i.e. the matrix of partial derivatives of model output with respect to model parameters  $p$ ), and  $Cov(p)$  the covariance matrix of parameter uncertainty, the covariance matrix of  $T_b$  uncertainties due to absorption-model parameters is computed as:

$$Cov(T_b) = K_p Cov(p) K_p^T \quad (13)$$

where  $T$  indicates the matrix transpose. Fig. 17 shows the  $T_b$  uncertainty due to uncertainties in SD parameters, in terms of the square root of the diagonal terms of  $Cov(T_b)$  for both vertically downwelling and upwelling geometry.

The two panels of Fig. 17 show that the contribution of SD parameters to the  $T_b$  uncertainty is fairly small, indicatively lower than a tenth of a Kelvin throughout the frequency range and atmospheric conditions for both downwelling and upwelling  $T_b$ . Conversely, other spectroscopic parameters, in particular those related to water-vapor (WV) continuum and 183-GHz line intensity, contribute more substantially to the uncertainty of  $T_b$  simulations. To demonstrate this, we performed a sensitivity study, as described in Cimini et al. [16], and selected the five most relevant parameters

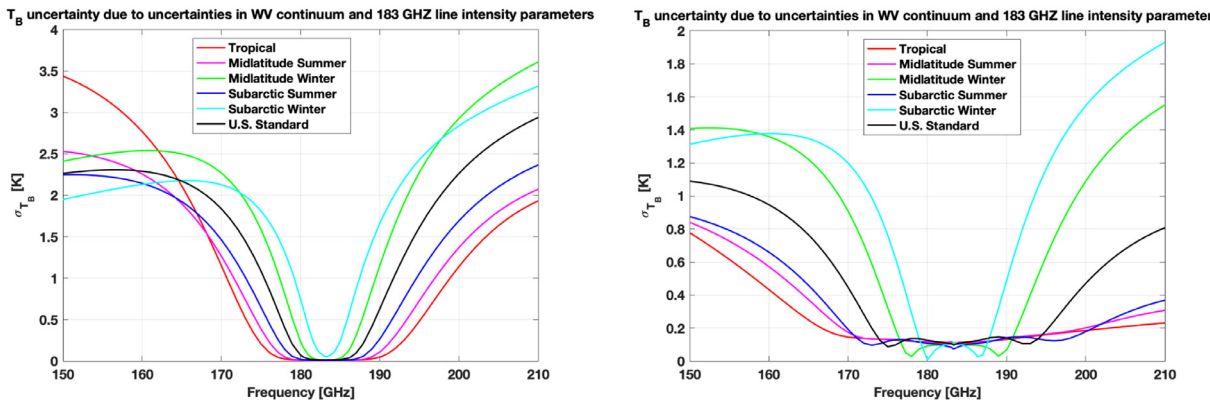


**Fig. 18.**  $T_b$  uncertainty ( $\sigma(T_b)$ ) due to the uncertainty in WV continuum and 183-GHz line intensity parameters. Six climatological atmospheric conditions (color-coded) have been used to compute  $K_p$ . Left: Vertically downwelling  $T_b$ . Right: Vertically upwelling  $T_b$ .

to be considered for computing the uncertainty impact. The resulting five parameters are: WV continuum self- ( $C_s$ ) and foreign- ( $C_f$ ) pressure induced coefficients and their temperature-dependence exponents ( $n_{C_s}$ ,  $n_{C_f}$ ), and line integrated intensity ( $S_i$ ). The full covariance matrix for these parameters has been estimated following [16], and the corresponding covariance matrix of  $T_b$  uncertainties was computed. The  $T_b$  uncertainty due to uncertainties in the above five parameters is reported in Fig. 18, similarly to Fig. 17.

It is evident that the uncertainty contribution of the continuum and line intensity parameters largely exceeds that of SD parameters, especially on the line wings.

## 7. Discussion and conclusions

As follows from the previous section, further improvement in the accuracy of atmospheric water-vapor retrieval will require revision of the line intensity and the water-vapor continuum. Experimental refinement of the corresponding parameters is feasible. That assumes the use of a cavity ring-down spectrometer (CRDS) or resonator spectrometer, since only such types of instruments can measure an absorption coefficient with the necessary accuracy. For example, Fleisher et al. [84] reports CRDS measurements of CO<sub>2</sub> line intensity in the infrared range with unprecedented uncertainty of 0.06%. The main difficulty of a similar study of the 183-GHz H<sub>2</sub>O line is a strong correlation between line intensity and coefficients of the underlying continuum, if these parameters are retrieved from fitting the model to the total observed absorption. Moreover, the continuum spectrum is not smooth in the vicinity of the line due to water-dimer rotational structure (see from [24] and references therein) which limits the signal-to-noise ratio and worsens the accuracy of the line parameters' retrieval. To avoid these problems, the line-profile recordings should be performed at pressures such that the continuum absorption is negligible. This range of pressures is usually not used in the microwave range, because it requires mechanical adjustment of the cavity length at each frequency step, which leads to significant complication in the spectrometer construction and measurement method. The problem can be resolved if the line's integrated intensity becomes available from ab initio calculations with sub-percent uncertainty. Such calculations seem feasible (see, e.g. [85]). The line intensity obtained from such calculations would allow removing the line profile from the observed spectrum and refining the continuum parameters.

In conclusion let us highlight the main findings of this work. We performed a state-of-the-art experimental and theoretical study of collisional parameters of one of the two most important microwave diagnostic lines used in remote sensing of atmospheric water vapor. The measurements thus obtained are in good agree-

ment with previously known values, but have smaller uncertainty. The data include the first measurement of speed-dependent collisional broadening and shifting of the 183-GHz line for both self- and air-broadening in the temperature range from about 220 to 360 K. Supporting calculations of the line parameters using the MCRB approach were performed for temperatures ranging from 200 to 3000 K. There is very good general agreement between measured and calculated broadening parameters and their temperature dependencies, but the study revealed difficulties in accurate calculations of line shifting, although its temperature dependence is reproduced rather well. The agreement between calculated and measured shifts is better for the H<sub>2</sub>O-air collision system than for H<sub>2</sub>O-H<sub>2</sub>O, which is probably due to a much more complex interaction potential in the latter case. In contrast to the line shift value, the calculations reproduce very well the impact of the SD effect. The agreement within measurement uncertainty between measured and calculated parameters  $\gamma_2$  and  $\delta_2$  for both air- and self-broadening, including their temperature dependence, confirms the capability of quantitative theoretical evaluation of this weak collisional effect. The impact of the updated spectroscopic parameters on radiative-transfer calculations and atmospheric water-vapor retrievals is calculated. We demonstrate that consideration of the SD effect is necessary for accurate estimation of water amount with this line, especially for the case of ground-based or limb-scanning radiometry. Non-negligible systematic errors (1–2%) are introduced if SD is neglected. Finally, we analyzed the contribution of spectroscopic parameters uncertainties to the uncertainty of radiative-transfer calculations and thus atmospheric water-vapor retrievals. It shows that the line's integrated intensity and water-vapor continuum parameters are the major contributors to the uncertainty of atmospheric water-vapor retrievals and thus shall be considered of primary importance for further specialized laboratory studies.

## Declaration of Competing Interest

The authors declare that they have no known competing financial interests or personal relationships that could have appeared to influence the work reported in this paper.

## CRedit authorship contribution statement

**M.A. Koshelev:** Methodology, Formal analysis, Writing - original draft, Writing - review & editing. **I.N. Vilkov:** Investigation, Data curation. **D.S. Makarov:** Visualization, Software. **M.Yu. Tretyakov:** Supervision, Conceptualization, Writing - review & editing. **B. Vispoel:** Formal analysis, Software. **R.R. Gamache:** Methodology, Software, Formal analysis, Writing - original draft. **D. Cimini:** Validation, Visualization, Writing - original draft. **F. Romano:** Formal

analysis, Software. **P.W. Rosenkranz:** Conceptualization, Writing - review & editing.

## Acknowledgements

Spectra recording and analysis was supported by the Russian Science Foundation (project 17-19-01602). Evaluation of the data impact in atmospheric applications was supported in part by EUMETSAT project ComboCloud (contract EUM/CO/19/4600002352/THH) and Russian State Project no. 0035-2019-0016.

## References

- [1] Cimini D, Westwater ER, Gasiewski AJ, Klein M, Leuski VY, Liljegren JC. Ground-based millimeter- and submillimeter-wave observations of low vapor and liquid water contents. *IEEE Trans Geosci Remote Sens* 2007;45(7):2169–80.
- [2] Cadeddu MP, Turner DD, Liljegren JC. A neural network for real-time retrievals of PWV and LWP from arctic millimeter-wave ground-based observations. *IEEE Trans Geosci Remote Sens* 2009;47(7):1887–900.
- [3] Ricaud P, Gabard B, Derrien S, Attie J, Rose T, Czekala H. Validation of tropospheric water vapor as measured by the 183-GHz HAMSTRAD radiometer over the Pyrenees mountains, France. *IEEE Trans Geosci Remote Sens* 2010;48(5):2189–203.
- [4] Wang JR, Racette PE, Piepmeier JRE, Monosmith B, Manning W. Airborne Co-S-MIR observations between 50 and 183 GHz over snow-covered Sierra mountains. *IEEE Trans Geosci Remote Sens* 2007;45(1):55–61.
- [5] Mech M, Orlando E, Crewell S, Ament F, Hirsch L, Hagen M, et al. HAMP—the microwave package on the high altitude and long range research aircraft (HALO). *Atmos Meas Tech* 2014;7(12):4539–53. doi:10.5194/amt-7-4539-2014.
- [6] Galin I, Brest DH, Martner GR. DMSP SSM/T-2 microwave water vapor profiler. In: Shiu JC, editor. Microwave instrumentation for remote sensing of the earth, 1995. International Society for Optics and Photonics: SPIE; 1993. p. 189–98. doi:10.1117/12.152603.
- [7] Blackwell WJ, Braun S, Bennartz R, Velden C, DeMaria M, Atlas R, et al. An overview of the TROPICS NASA earth venture mission. *Q J R Meteorol Soc* 2018;144(S1):16–26. doi:10.1002/qj.3290.
- [8] Reising SC, Gaier TC, Padmanabhan S, Lim BH, Heneghan C, Kummerow CD, et al. An earth venture in-space technology demonstration mission for temporal experiment for storms and tropical systems (tempest). In: IGARSS 2018 – 2018 IEEE international geoscience and remote sensing symposium; 2018. p. 6301–3.
- [9] Geer A, Baordo F, Bormann N, English S. All-sky assimilation of microwave humidity sounders 2014;ECMWF technical memorandum 721. <http://www.ecmwf.int/en/elibrary/technical-memoranda>.
- [10] Clain G, Brogniez H, Payne VH, John VO, Luo M. An assessment of SAPHIR calibration using quality tropical soundings. *J Atmos Ocean Technol* 2015;32(1):61–78. doi:10.1175/JTECH-D-14-00054.1.
- [11] Kobayashi S, Poli P, John VO. Characterisation of special sensor microwave water vapor profiler (SSM/T-2) radiances using radiative transfer simulations from global atmospheric reanalyses. *Adv Space Res* 2017;59(4):917–35. doi:10.1016/j.asr.2016.11.017.
- [12] Brogniez H, English S, Mahfouf J-F, Behrendt A, Berg W, Boukabara S, et al. A review of sources of systematic errors and uncertainties in observations and simulations at 183 GHz. *Atmos Meas Tech* 2016;9(5):2207–21. doi:10.5194/amt-9-2207-2016.
- [13] Bobryshev O, Buehler SA, John VO, Brath M, Brogniez H. Is there really a closure gap between 183.31-GHz satellite passive microwave and in situ radiosonde water vapor measurements? *IEEE Trans Geosci Remote Sens* 2018;56(5):2904–10.
- [14] Tretyakov MYu. Spectroscopy underlying microwave remote sensing of atmospheric water vapor. *J Mol Spectrosc* 2016;328:7–26. doi:10.1016/j.jms.2016.06.006.
- [15] Rosenkranz PW, Cimini D. Speed dependence of 22- and 118-GHz line shapes for tropospheric remote sensing. *IEEE Trans Geosci Remote Sens* 2019;57(12):9702–8.
- [16] Cimini D, Rosenkranz PW, Tretyakov MYu, Koshelev MA, Romano F. Uncertainty of atmospheric microwave absorption model: impact on ground-based radiometer simulations and retrievals. *Atmos Chem Phys* 2018;18(20):15231–59. doi:10.5194/acp-18-15231-2018.
- [17] Tran H, Bermejo D, Domenech J-L, Joubert P, Gamache R, Hartmann J-M. Collisional parameters of  $H_2O$  lines: Velocity effects on the line-shape. *J Quant Spectrosc Radiat Transf* 2007;108(1):126–45. doi:10.1016/j.jqsrt.2007.03.009.
- [18] Ngo NH, Tran H, Gamache RR, Bermejo D, Domenech J-L. Influence of velocity effects on the shape of  $N_2$  (and air) broadened  $H_2O$  lines revisited with classical molecular dynamics simulations. *J Chem Phys* 2012;137(6):064302. doi:10.1063/1.4739467.
- [19] Krupnov AF. Modern submillimetre microwave Scanning Spectrometry. In: Chantry GW, editor. Modern aspects of microwave spectroscopy. Academic Press Inc.; 1979. p. 217–56.
- [20] Ma Q, Tipping RH, Boulet C. Modification of the Robert-Bonamy formalism in calculating lorentzian half-widths and shifts. *J Quant Spectrosc Radiat Transf* 2007;103:588–96. doi:10.1016/j.jqsrt.2006.08.001.
- [21] Koshelev MA, Vilkov IN, Tretyakov MYu. Collisional broadening of oxygen fine structure lines: the impact of temperature. *J Quant Spectrosc Radiat Transf* 2016;169:91–5. doi:10.1016/j.jqsrt.2015.09.018.
- [22] Tretyakov MYu, Koshelev MA, Makarov DS, Tonkov MV. Precise measurements of collision parameters of spectral lines with a spectrometer with radioacoustic detection of absorption in the millimeter and submillimeter ranges. *Instrum Exp Tech* 2008;51(1):78–88.
- [23] Krupnov AF, Tretyakov MYu, Belov SP, Golubiatnikov GY, Parshin VV, Koshelev MA, et al. Accurate broadband rotational BWO-based spectroscopy. *J Mol Spectrosc* 2012;280:110–18. doi:10.1016/j.jms.2012.06.010.
- [24] Koshelev MA, Golubiatnikov GY, Vilkov IN, Tretyakov MYu. Line shape parameters of the 22-GHz water line for accurate modeling in atmospheric applications. *J Quant Spectrosc Radiat Transf* 2018;205:51–8. doi:10.1016/j.jqsrt.2017.09.032.
- [25] Koshelev MA, Tretyakov MYu, Rohart F, Bouanich J-P. Speed dependence of collisional relaxation in ground vibrational state of OCS: rotational behaviour. *J Chem Phys* 2012;136(12):124316. doi:10.1063/1.3696895.
- [26] Seleznev AF, Fedoseev GV, Koshelev MA, Tretyakov MYu. Shape of collision-broadened lines of carbon monoxide. *J Quant Spectrosc Radiat Transf* 2015;161:171–9. doi:10.1016/j.jqsrt.2015.04.011.
- [27] Koshelev MA, Delahaye T, Serov EA, Vilkov IN, Boulet C, Tretyakov MY. Accurate modeling of the diagnostic 118-GHz oxygen line for remote sensing of the atmosphere. *J Quant Spectrosc Radiat Transf* 2017;196:78–86. doi:10.1016/j.jqsrt.2017.03.043.
- [28] Ngo NH, Lisak D, Tran H, Hartmann J-M. An isolated line-shape model to go beyond the Voigt profile in spectroscopic databases and radiative transfer codes. *J Quant Spectrosc Radiat Transf* 2013;129:89–100. doi:10.1016/j.jqsrt.2013.05.034.
- [29] Rohart F, Mäder H, Nicolaisen H. Speed dependence of rotational relaxation induced by foreign gas collisions: Studies on  $CH_3F$  by millimeter wave coherent transients. *J Chem Phys* 1994;101(8):6475–86. doi:10.1063/1.468342.
- [30] Townes CH, Schawlow AL. *Microwave Spectroscopy*. Dover Publications; 1975. ISBN 9780486617985.
- [31] Demtroder W. *Laser spectroscopy: basic concepts and instrumentation*. Springer Berlin Heidelberg; 2002. ISBN 9783540652250.
- [32] Shirin SV, Zobov NF, Ovsyannikov RI, Polyansky OL, Tennyson J. Water line lists close to experimental accuracy using a spectroscopically determined potential energy surface for  $H_2^{16}O$ ,  $H_2^{17}O$ , and  $H_2^{18}O$ . *J Chem Phys* 2008;128(22):224306. doi:10.1063/1.2927903.
- [33] Renaud CL, Cleghorn K, Hartmann L, Vispoel B, Gamache RR. Line shape parameters for the  $H_2OH_2$  collision system for application to exoplanet and planetary atmospheres. *Icarus* 2018;306:275–84. doi:10.1016/j.icarus.2017.10.016.
- [34] Vispoel B, Cavalcanti JH, Gamache RR. Modified complex Robert-Bonamy calculations of line shape parameters and their temperature dependence for water vapor in collision with  $N_2$ . *J Quant Spectrosc Radiat Transf* 2019;228:79–89. doi:10.1016/j.jqsrt.2019.02.023.
- [35] Vispoel B, Cavalcanti JH, Paige ET, Gamache RR. Vibrational dependence, temperature dependence, and prediction of line shape parameters for the  $H_2O-N_2$  collision system. *J Quant Spectrosc Radiat Transf* 2020;253:107030. doi:10.1016/j.jqsrt.2020.107030.
- [36] Lamouroux J, Gamache R, Schwenke D. Determination of the reduced matrix elements using accurate ab initio wavefunctions: Formalism and its application to the vibrational ground state (000) of  $H_2^{16}O$ . *J Quant Spectrosc Radiat Transf* 2014;148:49–57. doi:10.1016/j.jqsrt.2014.06.011.
- [37] Gamache RR, Rey M, Vispoel B, Tyuterev VG. Reduced matrix elements for collisionally induced transitions of  $^{12}CH_4$ . *J Quant Spectrosc Radiat Transf* 2019;235:31–9. doi:10.1016/j.jqsrt.2019.06.010.
- [38] Gamache RR, Lynch R, Neshyba SP. New developments in the theory of pressure-broadening and pressure-shifting of spectral lines of  $H_2O$ : The complex Robert-Bonamy formalism. *J Quant Spectrosc Radiat Transf* 1998;59(3):319–35. doi:10.1016/S0022-4073(97)00123-4.
- [39] Shostak SL, Muenter JS. The dipole moment of water. II. Analysis of the vibrational dependence of the dipole moment in terms of a dipole moment function. *J Chem Phys* 1991;94(9):5883–90. doi:10.1063/1.460472.
- [40] Luo Y, Ågren H, Vahtera O, Jørgensen P, Spirko V, Hettema H. Frequency-dependent polarizabilities and first hyperpolarizabilities of  $H_2O$ . *J Chem Phys* 1993;98(9):7159–64. doi:10.1063/1.464733.
- [41] Gamache R, Fischer J. Half-widths of  $H_2^{16}O$ ,  $H_2^{18}O$ ,  $H_2^{17}O$ ,  $HD^{16}O$ , and  $D_2^{16}O$ : I. Comparison between isotopomers. *J Quant Spectrosc Radiat Transf* 2003;78:289–304.
- [42] Diaz Peña M, Pando C, Renuncio JAR. Combination rules for intermolecular potential parameters. I. Rules based on approximations for the long-range dispersion energy. *J Chem Phys* 1982;76(1):325–32. doi:10.1063/1.442726.
- [43] Diaz Peña M, Pando C, Renuncio JAR. Combination rules for intermolecular potential parameters. II. Rules based on approximations for the long-range dispersion energy and an atomic distortion model for the repulsive interactions.. *J Chem Phys* 1982;76(1):333–9. doi:10.1063/1.442727.
- [44] Gamache RR, Lamouroux J, Larai AL, Hartmann J-M, Boulet C. Semiclassical calculations of half-widths and line shifts for transitions in the 30012 ← 00001 and 30013 ← 00001 bands of  $CO_2$ . I: Collisions with  $N_2$ . *J Quant Spectrosc Radiat Transf* 2012;113(11):976–90. doi:10.1016/j.jqsrt.2012.02.014.
- [45] Lamouroux J, Gamache RR, Larai AL, Hartmann J-M, Boulet C. Semiclassical calculations of half-widths and line shifts for transitions in the 30012 ← 00001 and 30013 ← 00001 bands of  $CO_2$  II: Collisions with  $O_2$  and air. *J Quant Spectrosc Radiat Transf* 2012;113(11):991–1003. doi:10.1016/j.jqsrt.2012.02.015.
- [46] Lamouroux J, Gamache RR, Larai AL, Hartmann J-M, Boulet C. Semiclassical

- calculations of half-widths and line shifts for transitions in the 30012←00001 and 30013←00001 bands of CO<sub>2</sub>. III: Self collisions. *J Quant Spectrosc Radiat Transf* 2012;113(12):1536–46. doi:[10.1016/j.jqsrt.2012.03.035](https://doi.org/10.1016/j.jqsrt.2012.03.035).
- [47] Sack RA. Two-center expansion for the powers of the distance between two points. *J Math Phys* 1964;5(2):260–8. doi:[10.1063/1.1704116](https://doi.org/10.1063/1.1704116).
- [48] Flygare W, Benson R. The molecular Zeeman effect in diamagnetic molecules and the determination of molecular magnetic moments (*g* values), magnetic susceptibilities, and molecular quadrupole moments. *Mol Phys* 1971;20(2):225–50. doi:[10.1080/00268977100100221](https://doi.org/10.1080/00268977100100221).
- [49] Lide D. CRC handbook of chemistry and physics: a ready-reference book of chemical and physical data. CRC-Press; 1998. ISBN 9780849304798.
- [50] Mulder F, Dijk GV, Avoird AVD. Multipole moments, polarizabilities and anisotropic long range interaction coefficients for N<sub>2</sub>. *Mol Phys* 1980;39(2):407–25. doi:[10.1080/00268978000100341](https://doi.org/10.1080/00268978000100341).
- [51] Bogaard M, Orr B. MPT international review of science, physical chemistry, series two. Molecular Structure and Properties, 2. London: Butterworths; 1975. ISBN 0408706015.
- [52] Loftus A, Krupenie PH. The spectrum of molecular nitrogen. *J Phys Chem Ref Data* 1977;6(1):113–307. doi:[10.1063/1.555546](https://doi.org/10.1063/1.555546).
- [53] Stogryn DE, Stogryn AP. Molecular multipole moments. *Mol Phys* 1966;11(4):371–93. doi:[10.1080/00268976600101201](https://doi.org/10.1080/00268976600101201).
- [54] Hirschfelder JO, Curtiss CF, Bird RB. Molecular theory of gases and liquids. Wiley; 1955.
- [55] Koshelev M, Vilkov I, Tretyakov M. Temperature dependence of collisional parameters of water 183-GHz line. In: 25th international conference on high resolution molecular spectroscopy - abstract book; 2018. p. 232.
- [56] Golubiatnikov GYu. Shifting and broadening parameters of the water vapor 183-GHz line (3<sub>13</sub>-2<sub>20</sub>) by H<sub>2</sub>O, O<sub>2</sub>, N<sub>2</sub>, CO<sub>2</sub>, H<sub>2</sub>, He, Ne, Ar, and Kr at room temperature. *J Mol Spectrosc* 2005;230(2):196–8. doi:[10.1016/j.jms.2004.10.011](https://doi.org/10.1016/j.jms.2004.10.011).
- [57] Koshelev MA, Tretyakov MYu, Golubiatnikov GYu, Parshin VV, Markov VN, Koval IA. Broadening and shifting of the 321-, 325- and 380-GHz lines of water vapor by pressure of atmospheric gases. *J Mol Spectrosc* 2007;241:101–8. doi:[10.1016/j.jms.2006.11.005](https://doi.org/10.1016/j.jms.2006.11.005).
- [58] Pickett HM. Effects of velocity averaging on the shapes of absorption lines. *J Chem Phys* 1980;73(12):6090–4. doi:[10.1063/1.440145](https://doi.org/10.1063/1.440145).
- [59] Rohart F, Ellendt A, Kaghat F, Mäder H. Self and polar foreign gas line broadening and frequency shifting of CH<sub>3</sub>F: Effect of the speed dependence observed by millimeter-wave coherent transients. *J Mol Spectrosc* 1997;185(2):222–33. doi:[10.1006/jmsp.1997.7395](https://doi.org/10.1006/jmsp.1997.7395).
- [60] Hartmann J-M, Boulet C, Robert D. Collisional effects on molecular spectra: laboratory experiments and models, consequences for applications. Elsevier Science; 2008.
- [61] Tran H, Hartmann J-M. An isolated line-shape model based on the Keilson and Storer function for velocity changes. I. Theoretical approaches. *J Chem Phys* 2009;130(9):094301. doi:[10.1063/1.3073758](https://doi.org/10.1063/1.3073758).
- [62] Gamache RR, Vispoel B. On the temperature dependence of half-widths and line shifts for molecular transitions in the microwave and infrared regions. *J Quant Spectrosc Radiat Transf* 2018;217:440–52. doi:[10.1016/j.jqsrt.2018.05.019](https://doi.org/10.1016/j.jqsrt.2018.05.019).
- [63] Gordon IE, Rothman LS, Hill C, Kochanov RV, Tan Y, Bernath PF, et al. The HITRAN2016 molecular spectroscopic database. *J Quant Spectrosc Radiat Transf* 2017;203:3–69.
- [64] Frost BS. A theory of microwave lineshifts. *J Phys B* 1976;9(6):1001–20. doi:[10.1088/0022-3700/9/6/023](https://doi.org/10.1088/0022-3700/9/6/023).
- [65] Baldacchini G, Buffa G, D'Amato F, Pelagalli F, Tarrini O. Variations in the sign of the pressure-induced lineshifts in the v<sub>2</sub> band of ammonia with temperature. *J Quant Spectrosc Radiat Transf* 1996;55(6):741–3. doi:[10.1016/0022-4073\(95\)00187-5](https://doi.org/10.1016/0022-4073(95)00187-5).
- [66] Ulivi L, Lu Z, Tabisz GC. Temperature dependence of the collisional interference in the pure rotational far-infrared spectrum of HD. *Phys Rev A* 1989;40:642–51. doi:[10.1103/PhysRevA.40.642](https://doi.org/10.1103/PhysRevA.40.642).
- [67] Smith MAH, Rinsland CP, Devi VM, Benner DC. Temperature dependence of broadening and shifts of methane lines in the v<sub>4</sub> band. *Spectrochim Acta Part A* 1992;48(9):1257–72. doi:[10.1016/0584-8539\(92\)80263-V](https://doi.org/10.1016/0584-8539(92)80263-V).
- [68] Wilzewski JS, Birk M, Loos J, Wagner G. Temperature-dependence laws of absorption line shape parameters of the CO<sub>2</sub>v<sub>3</sub> band. *J Quant Spectrosc Radiat Transf* 2018;206:296–305. doi:[10.1016/j.jqsrt.2017.11.021](https://doi.org/10.1016/j.jqsrt.2017.11.021).
- [69] Cich MJ, Forthomme D, McRaven CP, Lopez GV, Hall GE, Sears TJ, et al. Temperature-dependent, nitrogen-perturbed line shape measurements in the v<sub>1</sub> + v<sub>3</sub> band of acetylene using a diode laser referenced to a frequency comb. *J Phys Chem A* 2013;117(50):13908–18. doi:[10.1021/jp408960e](https://doi.org/10.1021/jp408960e).
- [70] Goldenstein CS, Hanson RK. Diode-laser measurements of linestrength and temperature-dependent lineshape parameters for H<sub>2</sub>O transitions near 1.4 μm using Voigt, Rautian, Galatry, and speed-dependent Voigt profiles. *J Quant Spectrosc Radiat Transf* 2015;152:127–39. doi:[10.1016/j.jqsrt.2014.11.008](https://doi.org/10.1016/j.jqsrt.2014.11.008).
- [71] Stolarczyk N, Thibault F, Cybulski H, Jöwiak H, Kowzan G, Vispoel B, et al. Evaluation of different parameterizations of temperature dependences of the line-shape parameters based on *ab initio* calculations: case study for the HITRAN database. *J Quant Spectrosc Radiat Transf* 2020;240:106676. doi:[10.1016/j.jqsrt.2019.106676](https://doi.org/10.1016/j.jqsrt.2019.106676).
- [72] Bauer A, Godon M, Kheddar M, Hartmann J. Temperature and perturber dependences of water vapor line-broadening. Experiments at 183 GHz; calculations below 1000 GHz. *J Quant Spectrosc Radiat Transf* 1989;41(1):49–54. doi:[10.1016/0022-4073\(89\)90020-4](https://doi.org/10.1016/0022-4073(89)90020-4).
- [73] Goyette TM, De Lucia FC. The pressure broadening of the 3<sub>1,3</sub> – 2<sub>2,0</sub> transition of water between 80 and 600 K. *J Mol Spectrosc* 1990;143(2):346–58. doi:[10.1016/0022-2852\(91\)90099-V](https://doi.org/10.1016/0022-2852(91)90099-V).
- [74] Payne VH, Delamere JS, Clough SA. Air-broadened half-widths of the 22 GHz and 183 GHz water vapor lines. *IEEE Trans Geosci Remote Sens* 2008;46(11):3601–17.
- [75] Lisak D, Cygan A, Wcislo P, Ciurylo R. Quadratic speed dependence of collisional broadening and shifting for atmospheric applications. *J Quant Spectrosc Radiat Transf* 2015;151:43–8. doi:[10.1016/j.jqsrt.2014.08.016](https://doi.org/10.1016/j.jqsrt.2014.08.016).
- [76] Ghysels M, Liu Q, Fleisher AJ, Hodges JT. A variable-temperature cavity ring-down spectrometer with application to line shape analysis of CO<sub>2</sub> spectra in the 1600 nm region. *Appl Phys B* 2017;123(4):124. doi:[10.1007/s00340-017-6686-y](https://doi.org/10.1007/s00340-017-6686-y).
- [77] Rosenkranz PW. Line-by-line microwave radiative transfer (non-scattering). Remote Sens Code Libr <https://rscl-grss.org/coderecord.php?id=483>. 10.21982/M81013.
- [78] Van Vleck JH, Weisskopf VF. On the shape of collision-broadened lines. *Rev Mod Phys* 1945;17:227–36. doi:[10.1103/RevModPhys.17.227](https://doi.org/10.1103/RevModPhys.17.227).
- [79] Chevallier F, Di Michele S, McNally A.P. Diverse profile datasets from the ECMWF 91-level short-range forecasts. EUMETSAT NWP SAF Technical Report. [https://nwpsaf.eu/downloads/profiles/profiles\\_91L.pdf](https://nwpsaf.eu/downloads/profiles/profiles_91L.pdf).
- [80] NWP model profile data. <https://www.nwpsaf.eu/site/software/atmospheric-profile-data/>.
- [81] GVRP: G-band (183 GHz) vapor radiometer profiler. <https://www.arm.gov/capabilities/instruments/gvrp>.
- [82] Weng F, Zou X, Wang X, Yang S, Goldberg MD. Introduction to Suomi national polar-orbiting partnership advanced technology microwave sounder for numerical weather prediction and tropical cyclone applications. *J Geophys Res D* 2012;117(D19). doi:[10.1029/2012JD018144](https://doi.org/10.1029/2012JD018144).
- [83] Observing systems capability analysis and review tool, instrument: ATMS. <https://www.wmo-sat.info/oscar/instruments/view/53>.
- [84] Fleisher A, Adkins E, Reed Z, Yi H, Long D, Fleurbaey H, et al. Twenty-five-fold reduction in measurement uncertainty for a molecular line intensity. *Phys Rev Lett* 2019;123:043001. doi:[10.1103/PhysRevLett.123.043001](https://doi.org/10.1103/PhysRevLett.123.043001).
- [85] Polyansky O, Bielska K, Ghysels M, Lodi L, Zobov N, Hodges J, et al. High-accuracy CO<sub>2</sub> line intensities determined from theory and experiment. *Phys Rev Lett* 2015;114:243001. doi:[10.1103/PhysRevLett.114.243001](https://doi.org/10.1103/PhysRevLett.114.243001).